Three-dimensional discrete element simulation of indirect tensile behaviour of a transversely isotropic rock

Kaihui Li[a,b], Zhen-Yu Yin[a,*], Yungming Cheng[a], Ping Cao[b], Jingjing Meng[c]

Affiliation:

[a] Department of Civil and Environmental Engineering, The Hong Kong Polytechnic University, Hung Hom, Kowloon, Hong Kong, China

[b] School of Resources and Safety Engineering, Central South University, Changsha, Hunan 410083, China

c. Department of Civil, Environmental and Natural Resources Engineering, Lulea University of Technology, Luleå, Sweden.

* Corresponding author: Dr Zhen-Yu YIN, Tel: +85 3400-8470;

E-mail: zhenyu.yin@polyu.edu.hk; zhenyu.yin@gmail.com

Abstract: This paper presents the development of a three-dimensional discrete element model using flat-joint and smooth-joint contact models to investigate the effect of anisotropy on the tensile behaviour of slate, a transversely isotropic rock, under Brazilian testing from both macro and micro scales. The effect of anisotropy is further realised by exploring the influence of foliation orientations (β and ψ) on the tensile strength, fracture pattern, micro-cracking and stress distribution of the transversely isotropic rock. The variation of tensile strength with foliation orientation is presented. The cross-weak-plane fracture growth observed in laboratory is reproduced, and the criterion for which to form is also given from the aspect of foliation orientation. Furthermore, the proportional variations of micro-cracks well account for the effects of foliation orientation on the tensile strength and failure pattern. Finally, it is found that the existence of weak planes increases both the heterogeneity and the anisotropy of stress distributions within the transversely isotropic rock, with the degree of influence varying with the foliation orientation.

Keywords: transversely isotropic rock; foliation orientation; tensile strength; cross-weak-plane fracture; micro-crack

1. Introduction

Natural rocks are more or less anisotropic. The anisotropy in rocks is reflected by the different physical and mechanical properties in different directions. Typical anisotropic rocks include sedimentary rocks (shale, siltstone, claystone, sandstone, etc.) and metamorphic rocks (slate, phyllite, schist, gneiss, etc.). Because of their stratified or foliated structures, these rocks can further be treated as transversely isotropic material, in which one privileged direction exists and material behaviour has rotational symmetry with regard to that direction [1, 2]. Although the earth's crust is composed of approximately 95% igneous rocks and 5% sedimentary and metamorphic rocks, sedimentary and metamorphic rocks make up around 75% of the earth's surface [3]. As a result, transversely isotropic rocks are widely encountered in civil, mining, petroleum, geothermal, geo-environmental and radioactive waste disposal engineering [4-9].

The effect of anisotropy on the tensile behaviour of transversely isotropic rocks has been extensively studied for decades using analytical, experimental and numerical approaches [8, 10-21]. The published results have shown that the tensile behaviour of transversely isotropic rocks depends largely on the orientation of weakness planes (e.g., bedding plane and foliation plane) with respect to the loading direction. The Brazilian test is a most commonly used method of investigating the tensile strength and failure pattern of transversely isotropic rocks. Moreover, in most research, the sample is cored parallel to the orientation of weakness planes and the failure pattern under the Brazilian test is regarded as two-dimensional (2D). In fact, even though the strike of weakness planes coincides with the sample axis, the cross-weak-plane fracture is likely to be observed as illustrated in Figure 1. The results observed in slate indicate that failure patterns after Brazilian testing on both sides of the specimen are distinctly different and that the fracture section presents a cross-weak-plane structure when the loading-foliation angle is high. The likely reasons for the cross-weak-plane fracture growth are deviation of the strike direction of weakness planes from the sample axis, the ripple arrangement of the weakness planes, pyrite inclusion or other

imperfections [22]. The anisotropy is further demonstrated by the results of Brazilian tests observed in sandstone, gneiss and slate [23-25]. The Brazilian tensile strength and energy storage capacity were found to be associated with the orientation of weakness planes with respect to the directions of loading and sample axis. However, in these tests, some key information such as microcrack initiation, evolution and distribution in three-dimension is difficult to be obtained. The underlying failure mechanism of the transversely isotropic rock under Brazilian tests also remains poorly constrained.

Recently, many studies have focused on investigating the strength and deformation behaviour of transversely isotropic rocks by 2D numerical models combining bonded-particle and smooth-joint contact models [12, 18, 20, 26-31]. These studies revealed that the behaviour of weakness planes can be well reproduced by persistent [12, 27, 29, 30], non-persistent [18, 26, 31] or a mix of persistent with non-persistent smooth-joint contacts [20], depending on different microstructures of weakness planes embedded in rocks. Nevertheless, 2D modelling is incapable of analysing many practical anisotropic problems, including borehole instability in oblique wells excavated in anisotropic formations [5, 32], estimation of elastic properties for transversely isotropic rocks [33] and reproduction of cross-weak-plane fracture growth in transversely isotropic rocks of interest in this current study. To the authors' knowledge, there have been few reports on the three-dimensional (3D) modelling of tensile behaviour of the transversely isotropic rock in a Brazilian test, particularly considering the space orientation of weak planes.

To address the foregoing gaps, a three-dimensional DEM (Discrete Element Method) model of transversely isotropic rock was developed, with the main objective of exploring the effect of foliation orientation on rupture characteristics of slate during Brazilian tests. The particle-based DEM enables the tracking of crack initiation and propagation and rock failure at both the macro and micro scales [34-37]. The foliation orientation system is characterised by the foliation angle (ψ), which is the angle between the sample axis and foliation planes, and the loading-foliation angle (β), which is the angle between the loading direction and

foliation planes. Foliation planes with different ψ and β in the range of 0° to 90° at intervals of 15° were considered in the numerical modelling to cover a full spectrum of potential orientations.

2. Numerical approach

To simulate a transversely isotropic rock, two consecutive stages should be carried out: (1) modelling of the isotropic rock matrix and (2) modelling of the transversely isotropic weak planes [20, 27]. In the particle-based DEM, the rock matrix is represented by an assembly of rigid bonded particles, such as blocks or spheres, in three dimensions [38]. Based on the principles laid out in Li et al. [39], the flat-joint contact (FJC) model is adopted to simulate the rock matrix in this study, because it overcomes the three intrinsic problems: (a) low ratio of uniaxial compressive strength to tensile strength, (b) low internal friction angle and (c) linear strength envelope [40] in simulation of the hard rock when using the contact-bond or parallel-bond contact model. The behaviour of weak planes is modelled using the smooth-joint contact (SJC) model developed by Cundall [41]. A brief introduction to FJC and SJC models is presented in this section.

2.1 Flat-joint contact model

A flat-joint contact, which can be installed between grains with a gap less than the installation gap, and its corresponding flat-jointed material is presented in Figure 2. The installation gap is defined as

$$g = g_{ratio} \times \min(R_1, R_2) \tag{1}$$

where g is the installation gap; g_{ratio} is the installation gap ratio, which satisfies $0 \le g_{ratio} < R_{\min} / R_{\max}$ to prevent grains from being embedded in connecting pairs [42]; R_1 and R_2 are radii of the two interacting grains.

A flat-joint contact is consisted of a connecting interface and two rigid grains with skirted faces. The interface is discretized into $N_r \times N_\alpha$ elements (N_r and N_α are the number of elements in radial and circumferential directions respectively), each of which is bonded or unbonded. Combined the contributions of all elements, the interface presents an emergent behaviour evolving from a linear elastic and fully bonded to a partially damaged and finally to fully unbonded state. The strength envelopes of bonded and unbonded elements are shown in Figure 3a. The bonded element follows the Coulomb criterion with tension cutoff according to

$$\sigma^{(e)} \le \bar{\sigma}_b \tag{2}$$

$$\tau^{(e)} = \bar{c}_b - \sigma^{(e)} \tan(\bar{\phi}_b) \tag{3}$$

where $\sigma^{(e)}$ and $\tau^{(e)}$ are the applied normal and shear stresses on the element, respectively; $\sigma^{(e)} > 0$ represents tension; $\bar{\sigma}_b$, $\bar{c}_b$ and $\bar{\phi}_b$ are the bond tensile-strength, cohesion and friction angle, respectively. The bonded element breaks in either tensile or shear mode into the unbonded element when the corresponding strength limit is exceeded. The unbonded element can only bear a frictional force,

$$\tau^{(e)} = -\mu\sigma^{(e)} \tag{4}$$

Each element sustaining a force ($\mathbf{F}^{(e)}$) and moment ($\mathbf{M}^{(e)}$) at its centroid obeys the force-displacement law (see Fig. 3b) to update the force, moment and bond state. The force and moment are calculated as follows

$$\mathbf{F}^{(e)} = -F_n^{(e)}\mathbf{n_c} + \mathbf{F_s}^{(e)} \tag{5}$$

$$\mathbf{M}^{(e)} = M_t^{(e)}\mathbf{n_c} + \mathbf{M_b}^{(e)} \tag{6}$$

where $F_n^{(e)}$ represents the normal force and $F_n^{(e)} > 0$ denotes tension; $\mathbf{n_c}$ is the contact

unit-normal vector; $\mathbf{F}_{\mathbf{s}}^{(e)}$ represents the shear force vector; $\mathbf{M}_{\mathbf{b}}^{(e)}$ represents the bending moment vector, and $M_t^{(e)}$ is the twisting moment and assumed to be zero for simplification based on the assumption that shear stress caused by relative twist rotation keeps constant in the whole element so that the induced twisting moment at the element centroid is zero. The inaccuracy resulted from this simplification can be reduced by increasing the number of elements owned by individual FJC, while this increase will reduce the calculation efficiency [39].

Furthermore, the initial fraction of bonded contact (type B) and unbonded contact, including gapped (type G) and slit contacts (type S), within a synthetic rock matrix can be defined by varying parameters φ_B, φ_G and φ_S ($\varphi_B+\varphi_G+\varphi_S=1$). The previous parametric study demonstrated that the increase of g_{ratio} or/and φ_B strengthens the integrity of rock matrix [40]. Even after the FJC is broken, it can still resist the relative rotation due to its faced microstructure, which provides adequate interlocking that cannot be provided by spherical grains.

2.2 Smooth-joint contact model

A smooth-joint contact is installed between grains lying on opposite sides of the joint (weak plane), as shown in Figure 2. Grains joined by SJC move across instead of around each other by sliding along the weak plane with dilation. The strength envelope and force-displacement law of the SJC and the element of FJC follow a similar pattern as illustrated in Figure 3, but the macroscopic behaviours modelled by SJC and FJC are very different. The FJC presents a progressive failure, while the SJC presents a catastrophic failure. Moreover, the SJC does not resist the relative rotation. The force and displacement of SJC are updated as follows

$$\mathbf{F}=-F_n\mathbf{n}_j+F_s\mathbf{t}_j \tag{7}$$

$$\mathbf{U}=-U_n\mathbf{n}_j+U_s\mathbf{t}_j \tag{8}$$

where $\mathbf{F}$, F_n and F_s denote the force vector, normal and shear forces, respectively; $\mathbf{U}$, U_n and U_s denote the displacement vector, normal and shear displacements, respectively; $\mathbf{n}_j$ and $\mathbf{t}_j$ are the unit-vector normal and tangential to the weak plane, respectively.

For a bonded contact, if $F_n \geq \sigma_c A$, the bond breaks in tension (σ_c and A are the tensile strength and area of bond, respectively); if $F_s \geq \left(c_b - \sigma \tan\phi\right) A$, the bond breaks in shear (c_b and ϕ are the cohesion and friction angle of bond, respectively); otherwise, the bond remains intact. For an unbonded contact, if $F_s \leq -\mu_c \sigma A$, $F_s=-\mu_c F_n$ (μ_c is the friction coefficient of SJC); otherwise, slip tends to occur ($F_s=F_s'$) with an increase in normal force according to

$$\Delta F_n = \left(\frac{F_s' + \mu_c \sigma A}{\bar{k}_s} \right) \bar{k}_n \tan\left(\psi_c\right) \tag{9}$$

where $\bar{k}_n$, $\bar{k}_s$ and ψ_c are the normal stiffness, shear stiffness and dilation angle of SJC, respectively.

2.3 Generation of numerical specimen

A disk-shaped specimen (diameter = 50 mm and thickness = 25 mm) and a cylindrical specimen (diameter = 50 mm and length = 100 mm) were generated, comprising 29,290 and 116,029 particles connected by FJCs, respectively. The porosity of both specimens was fixed at a same value of 39.2 % using the particle deletion method [39, 43] to eliminate the influence of porosity, which produces substantial variations in strength and elasticity [44]. The particle size distributions of the two specimens were also identical, with a maximum to minimum particle diameter ratio of 1.5. The model resolution, defined as the average number of particles across the minimum diameter or length of specimen, was controlled by the disk-shaped specimen at

20 based on our previous study [39]. As seen in Figure 4 [45], the foliation planes in slate are persistent and parallel, so the behaviour of transversely isotropic slate was modelled by inserting a set of persistent and parallel weak planes into the isotropic rock matrix. The construction of the transversely isotropic rock model (FJC-SJC model) and the definitions of β and ψ are illustrated in Figure 2. For the disk-shaped specimen under Brazilian tests, β and ψ varied from 0° to 90° at intervals of 15°. Meanwhile, for the cylindrical specimen, with the loading direction coinciding with the sample axis under uniaxial compression tests ($\beta = \psi$), β was chosen to be 0°, 15°, 30°, 45°, 60° and 90°, in line with the experiment in the reference [46].

3. Numerical test

In this section, those micro-properties of FJC and SJC relevant for simulating the slate were calibrated against the experimental results obtained from uniaxial compression and Brazilian tests on samples having a diameter of 50 mm. In previous 2D modelling, the specimen at ψ = 90° was treated as isotropic, neglecting the influence of weak planes [12, 20, 26]. However, as shown in Figure 5, the experimental observation indicated the specimen at ψ = 90° after Brazilian testing split along the loading axis with additional failure planes developed in the direction of weak planes, which is very different from that for isotropic rocks. Accordingly, development of an appropriate calibration method for the 3D model is necessary.

3.1 Calibration procedure

The influence of micro-parameters of FJC and SJC on the macro behaviour of DEM models has been studied by Xu et al. [12, 30] from a 2D viewpoint. These studies can be important references with which to develop an appropriate calibration procedure for 3D DEM models of the transversely isotropic rock. As shown by the experimental results [46], the minimum uniaxial compressive strength (UCS) occurs at β = 30°–45°, and the cohesion and friction angle of the foliation plane are taken as their averages: 23 MPa and 35°, respectively. Hence

the first approximations of cohesion (σ_c) and friction coefficient (μ_c) of SJC are 23 MPa and 0.7, respectively. A new calibration procedure is proposed, as shown in flowchart form in Figure 6, that can be described by the following steps:

Step 1: The stiffness of SJC has little effect on the Young's modulus (E_0) of specimen when β = 0° under uniaxial compression. Thus the deformation parameters ($E_c, \bar{E}_c, k^n, k^s, \bar{k}^n, \bar{k}^s$) of both particle and FJC were adjusted to match E_0 through uniaxial compression tests.

Step 2: When β = 90°, the Young's modulus (E_{90}) of specimen depends primarily on the stiffness of SJC and the uniaxial compressive strength (UCS_{90}) of specimen is well correlated to the cohesion of FJC. Hence both E_{90} and UCS_{90} of the specimen were calibrated through adjustment of the deformation parameters ($\bar{k}_n$, $\bar{k}_s$) of SJC and the cohesion ($\bar{c}_b$) of FJC, respectively, by conducting uniaxial compression tests.

Step 3: Because the strength of SJC has little effect on the tensile failure strength ($\sigma_{t\_\psi=90^\circ}$) of specimen at $\psi = 90°$, the tensile strength ($\bar{\sigma}_b$) of FJC was iteratively adjusted to match $\sigma_{t\_\psi=90^\circ}$ by Brazilian tests.

Step 4: The tensile failure strength ($\sigma_{t\_\psi=0^\circ,\beta=0^\circ}$) of specimen at ψ = 0° and β = 0° is largely determined by the tensile strength (σ_c) of SJC, whereas that ($\sigma_{t\_\psi=0^\circ,\beta=90^\circ}$) at ψ = 0° and $\beta = 90°$ is closely related to the cohesion (c_b) of SJC. Accordingly, two separate series of Brazilian tests on specimens at $\psi = 0°, \beta = 0°$ and $\psi = 0°, \beta = 90°$ were performed to calibrate σ_c and c_b, respectively.

3.2 Calibration results

Following the flowchart shown in Figure 6, the micro-parameters of FJC and SJC for simulating the slate were calibrated as listed in Table 1 and 2. Notably, the slit element fraction ($\varphi_S = 1-\varphi_B-\varphi_G$), regarded as the quantification of crack density [40], was chosen to be 0.1 so as to take into account the randomly distributed pre-existing cracks in the slate. The combination of $N_r \times N_\alpha = 1\times 4$ has been validated to be best suited for calculation efficiency [39]. For simplicity, the normal stiffness and shear stiffness of SJC are set to be equal, as in previous studies [12, 18, 19, 28, 30, 31]. The value of the micro-tensile strength of SJC (3.5 MPa) is lower than the macro-tensile strength (6.0 MPa as shown in Figure 7c) of the disk-shaped specimen at ψ = 0°, β = 0°, because the micro-tensile cracks along the SJC were initiated prior to the peak of the macro-tensile strength of the specimen, consistent with the findings in Park and Min [27] and Park et al. [47].

The conventional formula for calculating the indirect tensile strength (σ_t) based on Brazilian tests is

$$\sigma_t = \frac{2F}{\pi Dt} \tag{10}$$

where F is the force at failure, and D and t are the diameter and thickness of the disk-shaped specimen, respectively. Two prerequisites for this formula are that (1) the material be isotropic and (2) the fracture be initiated by tensile crack from the centre of the disk-shaped specimen. For the transversely isotropic rock of interest in this research, the strength obtained from this formula cannot represent the true tensile strength for most cases. Accordingly, the phrase *Brazilian failure strength (BFS)* rather than *Brazilian tensile strength (BTS)* will be used to describe the result of Eq. (10). The UCS and apparent Young's modulus of slate specimens at β = ψ in the range of 0°~90° under uniaxial compressive condition and BFS of slate specimens at ψ = 0°, β = 0°~90° under Brazilian tensile condition obtained from the

experimental and numerical tests are comparable as illustrated in Figure 7. Additionally, the influence of foliation spacing on BFS, associated with the loading-foliation angle, is shown in Figure 7d. The foliation spacing of 5.0 mm is adopted due to the good agreement between numerical and experimental results. Consequently, these results indicate that the proposed 3D DEM model is well calibrated to capture the mechanical behaviour of the transversely isotropic slate.

3.3 Parametric study

Based on the calibrated micro-parameters, the numerical specimen having different foliation orientations (β and ψ) were created and subjected to Brazilian tests. ψ and β covered a range of 0° to 90° at intervals of 15°. The loading velocity for the Brazilian test simulation was controlled at 0.015 m/s – slow enough to ensure the specimen being in a quasi-static equilibrium for each step. 57 measurement spheres with diameter l = 2.5 mm, containing approximately 5 particles apiece, were installed along the loading plane of the disk-shaped specimen. As shown in Figure 8, these measurement spheres were arranged in three columns, located in the middle plane, near the front and rear surfaces. It should be noted that stress is a physical quantity in continuum mechanics and does not actually exist anywhere in the particle assembly owing to the discreteness of DEM model [34]. To bridge this gap between the microscale and a continuum, an averaging procedure is adopted [48]. The stress at one point is taken as the average in a measurement region, a measurement sphere in this study, with a volume V according to

$$\bar{\sigma} = -\frac{1}{V}\sum_{N_c} \mathbf{F}^{(c)} \otimes \mathbf{L}^{(c)} \tag{11}$$

where N_c is the number of contacts within the measurement region; $\mathbf{F}^{(c)}$ and $\mathbf{L}^{(c)}$ denote the contact vector and the branch vector connecting the centroids of the two contact ends, respectively. Accordingly, the diameter of measurement spheres cannot be too large to accurately reproduce the stress at one particular point. In this way, stresses and strains along

the loaded diameter on end surfaces and middle plane of the disk-shaped specimen were monitored throughout the test.

4. Results and discussion

4.1 Tensile strength

Considering the elastic constants, Claesson and Bohloli [15] proposed a reasonably accurate approximate formula for calculating the tensile strength of transversely isotropic rocks,

$$\sigma_t = \frac{2P}{\pi D t}\left[(\sqrt[4]{E/E'})^{(-\cos 2\beta)} - \frac{\cos 4\beta}{4}(b-1)\right]$$
$$b = \frac{\sqrt{EE'}}{2}\left(\frac{1}{G'} - \frac{2\nu'}{E'}\right) \quad (12)$$

where E and E' are the elastic moduli parallel to and normal to the transversely isotropic plane, respectively, and G' and ν' represent the shear modulus and the Poisson's ratio in the direction perpendicular to the plane of transverse isotropy, respectively. Because this formula only takes the loading-foliation angle into consideration by postulating the strike of weak planes parallel to the sample axis ($\psi = 0°$), its applicability to transversely isotropic rocks remains open to question when $\psi \neq 0°$ [25]. Accordingly, further research, that goes beyond the scope of this study, into this issue is needed.

The tensile strength of slate samples at $\psi = 0°$ was obtained by Eq. (12) based on experimental results [45]. The tensile stress (σ_{xx}) at the centre of specimen at failure is usually regarded as the tensile strength of a specimen per Claesson and Bohloli [15] and Yu et al. [49], taking the average of σ_{xx} measured by three measurement spheres installed at the centre (see Figure 8) in numerical tests. Along with the distribution of lab results, numerical BFS and σ_{xx} at the centre as a function of β are compared as shown in Figure 9. The result indicates that both numerical BFS and σ_{xx} at the centre can reasonably accurately represent the tensile strength

of a specimen, but the numerical BFS seems more appropriate than σ_{xx} at the centre from the viewpoint of the overall trend. Consequently, BFS based on Eq. (10) is used hereinafter to study the influence of foliation orientation on the tensile strength.

Figure 10 shows the influences of β and ψ on BFS of numerical specimen. When $0° \le \psi \le 30°$, as shown in Figure 10a, values of BFS at each β are very similar, implying that the BFS of numerical specimen depends primarily on β rather than on ψ, and they increase gradually with β. When $45° \le \psi \le 90°$, the variation of BFS is insensitive to β, and values of BFS increase with ψ, as illustrated in Figure 10b. Furthermore, the effects of β and ψ on the anisotropy of BFS is investigated by normalizing the results to 1 at $\psi = 0°$ and $\beta = 0°$. As seen in Figure 11, at $45° \le \psi \le 90°$, the variation of anisotropy ratio with β and ψ obtained by this study is similar to those obtained by Ding et al. [25] and Dan et al. [23], which exhibits an ascending trend with ψ and is nearly independent of β. However, the results are different at $0° \le \psi < 45°$ in these three studies. For instance, in our research, the anisotropy ratio of BFS generally increases with β at $0° \le \psi \le 30°$, and the coupling effect of β and ψ is evident at $30° \le \psi < 45°$. For results of Ding et al., the coupling effect of β and ψ on the anisotropy ratio of BFS is dominant at this range. In relation to results of Ding et al., the anisotropy ratio of BFS grows as ψ increases at $0° \le \psi < 45°$ and $0° \le \beta \le 30°$, and the coupling effect plays a role in the rest of β and ψ. Overall, the BFS of slate samples presents evident anisotropic variation, with the values of anisotropy ratio of BFS reaching 3.58, 2.85 and 5.24 for this study, Ding et al. [25] and Dan et al. [23], respectively.

Tavallali and Vervoort [16] found that the micro-scale properties of one layered sandstone collected from different locations can be very different. Furthermore, the difference of micro-scale properties (e.g. mineral content, grain size and thickness of layer boundaries) in the transversely isotropic rock results in different macro-scale behaviours, including tensile strength and failure pattern, of samples under Brazilian tests [16]. Therefore, it can be inferred that the above-mentioned difference in anisotropy ratio of BFS is attributed to the different micro-scale properties of slate samples obtained from three different places. However, it seems a general rule to slate that the anisotropy ratio of BFS increases with ψ when $45° \le \psi \le 90°$.

4.2 Fracture pattern

In the particle-based DEM, micro-cracks can be monitored and counted during the fracture process to analyse the damage evolution. When the local stress acting on the contact exceeds the pre-setting strength, it breaks in a tensile or shear fashion and produces one micro-crack. In our transversely isotropic rock modelling, four types of micro-cracks are generated: tensile and shear cracks in the rock matrix and weak planes. Due to the page limit, Figure 12 shows only the stress and micro-crack evolution of specimens at foliation orientations (ψ–β) of 0°–0°, 0°–45°, 0°–90°, 45°–0°, 45°–45°, 45°–90° and 90°–45° under Brazilian tests. Some critical points (*a*, *b*, *c* and *d*) and their corresponding damage location and degree are also displayed in Figure 12.

At ψ–β = 0°–0°, the tensile cracks in weak planes initiate at the centre (point *a*) and propagate towards the top and bottom loading points; after the peak stress of point *b*, secondary cracks appear near the loading points along the weak planes and grow towards the centre of the disk. The damage of numerical specimen is dominated by the tensile cracks in weak planes.

At ψ–β = 0°–45°, at first, few sporadic micro-cracks are noticed (point *a*); and then the tensile cracks in the rock matrix and shear cracks in weak planes increase at the same level, concentrated at the loading points (point *b*); last, the tensile cracks in the rock matrix and weak planes increase rapidly and the number of tensile cracks in weak planes exceeds that of the shear cracks in weak planes. The fracture begins at the loading points and propagates along the weak planes (point *c*), then propagates across the weak planes in the rock matrix, forming an arc-shaped macro-fracture (point *d*).

At ψ–β = 0°–90°, there exist stress fluctuations (point *b*) occurring, with tensile cracks in the rock matrix increasing at a high rate and shear cracks in weak planes increasing at a low rate; fracture of the numerical specimen starts from the top and bottom loading points and evolves towards the centre of the disk; ultimately the numerical specimen fails by the tensile cracks through the rock matrix, accompanying secondary cracks along the weak planes concentrated

at the loading points.

When the strike of weak planes coincides with the sample axis ($\psi = 0°$), the fracture pattern of the numerical specimen is largely dependent of β and in line with the experimental results. The variation of fracture process with β is also consistent with the laboratory observations as shown in Figure 13, which depicts the stress-strain curves and failure patterns of slate specimens at different loading directions. The transverse strains (No. 4 to 8) along the loaded diameter of specimen were measured by a series of horizontal strain gages with a length of 20 mm, long enough to capture the fracture initiation point within the specimen. Accordingly, based on the maximum extension strain criterion that the failure occurs if the extension (tensile) strain exceeds the allowable strain [50], the fracture process can be summarized as follows: the specimen at $\beta = 0°$ tends to fail starting from the disk center, while at other values of β the specimen tends to fail starting from the loading points where the largest transverse strain first arrives. Moreover, the cross-weak-plane fracture growth is not common in numerical specimens at $\psi = 0°$.

At ψ–β = 45°–0°, nearly no micro-cracks appear at first, and then the tensile cracks in weak planes increase rapidly in a stepped fashion and the tensile cracks in the rock matrix increase at a relatively low rate; last, the tensile cracks in weak planes increase at a relatively low rate but the tensile cracks in the rock matrix increase at a high rate, although both reach the same level by the point of ultimate stress. The fracture of the numerical specimen starts from the centre of the disk, along the weak planes, and propagates towards the loading points, accompanying cracks forming in the rock matrix near the loading points (point *c*), after which the cracks in the rock matrix grow from the two loading points to the centre of the disk. Seen from the bottom view, the fracture formed in the rock matrix is aligned with the direction of the sample axis, being inclined to the fracture induced in the weak planes (point *d*). Hence, the fractures formed in rock matrix and weak planes make up a cross-weak-plane fracture.

At ψ–β = 45°–45°, at first, the tensile cracks in the rock matrix and shear cracks in weak planes increase at the same level; afterwards, the tensile cracks in the rock matrix, shear and

tensile cracks in weak planes grow at a higher rate. The fracture of numerical specimen begins at the loading points by simultaneous appearance of shear cracks along the weak planes and of tensile cracks in the rock matrix (point *b*), then propagates towards the centre of the disk (point *c*). At the ultimate stage, a cross-weak-plane fracture, that a shear fracture goes through the rock matrix and connects three tensile fractures formed in the weak planes, is formed (point *d*).

At ψ–β = 45°–90°, the tensile cracks in the rock matrix, shear and tensile cracks in weak planes evolve in a pattern similar to that seen at ψ–β = 45°–45°. However, their fracture patterns are very different. At β = 90°, the fragments of numerical specimen formed by intersecting cracks along the weak planes with those in rock matrix at the loading points, are spalled from the specimen, leaving its centre part still intact after testing.

Finally, at ψ = 90° is a special case in which the fracture pattern of the numerical specimen is independent of β because the loading direction is inherently parallel to the weak planes. Fracture of the numerical specimen begins simultaneously at the loading points by tensile cracks in the rock matrix and weak planes and propagates towards the centre of specimen until the crack coalescence. The cracks in the rock matrix and along weak planes intersect perpendicular to each other.

Combining all the cases, it can be concluded that the fracture pattern of slate specimen in a Brazilian test primarily depends on ψ, while its fracture process is largely dependent on β. The cross-weak-plane fracture growth is significant in specimens at $30° \le \psi \le 60°$, but in other cases ($0° \le \psi \le 15°$ and $75° \le \psi \le 90°$) it is slight. The fracture of specimen at $0° \le \psi \le 60°$ and $0° \le \beta \le 15°$ initiates at the centre of the disk and then propagates towards the loading points, whereas the specimen presents an opposite fracture process in other cases.

4.3 Micro-crack proportion

To obtain a better understanding of the influence of micro-crack type on fracture pattern, the ratios of the tensile and shear cracks in the rock matrix and weak planes to all cracks are

calculated at failure. The proportional variations of micro-cracks at different ψ and β are shown in Figure 14. The proportional variations of micro-cracks at ψ = 0°–30° are similar, implying the absence of influence imposed by ψ. The portion of tensile cracks in the rock matrix increases continuously with increasing β, and the portion of shear cracks in the rock matrix is minimal irrespective of β. At $0° \le \beta \le 15°$, the very high portion of tensile cracks in weak planes indicates that the numerical specimen fails by tension along the weak plane. With β increasing, the tensile cracks in weak planes tend to disappear. Meanwhile, at $30° \le \beta \le 90°$, the portion of shear cracks in weak planes gradually decreases with β, with the tensile fracture in the rock matrix dominating at $75° \le \beta \le 90°$. At $30° \le \beta \le 60°$, the portions of tensile cracks in the rock matrix and shear cracks in weak planes are comparable, indicating that the numerical specimen fails by a mixed shear along the weak plane with tensile across the rock matrix fracture, consistent with laboratory observations (Figure 13).

Additionally, at ψ = 45°–75°, the most distinct difference between proportional variations of micro-cracks from those at ψ = 0°–30° is that the portions of tensile cracks in the rock matrix are nearly constant at $30° \le \beta \le 90°$. This can explain why the BFS of numerical specimen is insensitive to β in this range of ψ. Furthermore, the level of portion of tensile cracks in the rock matrix increases with ψ, which can be used to account for the increased BFS. At ψ = 90° is a special case in which the proportional variation of micro-cracks is independent of β, with tensile cracks in the rock matrix and weak planes dominating the failure of the numerical specimen. Although the portion of tensile cracks in the rock matrix at ψ = 90° is not the highest seen, the corresponding BFS is. This can be attributed to a special failure mode in which the numerical specimen fails by tensile splitting through the rock matrix along the loading direction, behaving like an intact specimen without weak planes. The effective portion of tensile cracks in the rock matrix is far higher when excluding the cracks in weak planes. Thus, the tensile strength of specimen correlates positively to the portion of tensile cracks formed in the rock matrix.

4.4 Principal stress distribution

The effect of foliation orientation on principal stress distribution along the loaded diameter is further explored in this section. Based on the assumption that a material is homogeneous, isotropic and linear elastic, Hondros [51] proposed a 2D stress solution for the specimen under the diametric loading over finite arcs according to,

$$\sigma_{\theta\theta}=\frac{P}{\pi Rt\alpha}\left\{\frac{\left[1-\left(r/R\right)^2\right]\sin 2\alpha}{1-2\left(r/R\right)^2\cos 2\alpha+\left(r/R\right)^4}-\tan^{-1}\left[\frac{1+\left(r/R\right)^2}{1-\left(r/R\right)^2}\tan\alpha\right]\right\} \tag{13}$$

$$\sigma_{rr}=-\frac{P}{\pi Rt\alpha}\left\{\frac{\left[1-\left(r/R\right)^2\right]\sin 2\alpha}{1-2\left(r/R\right)^2\cos 2\alpha+\left(r/R\right)^4}+\tan^{-1}\left[\frac{1+\left(r/R\right)^2}{1-\left(r/R\right)^2}\tan\alpha\right]\right\} \tag{14}$$

where $\sigma_{\theta\theta}$ and σ_{rr} represent the principal stresses in the tangential and radial directions, respectively; P is the exerted force; R and t are the radius and thickness of the disk-shaped specimen, respectively; 2α is the arc over which the force is applied; and r is the distance from the centre of the disk. Notably, tensile stress is regarded as positive. This analytical solution is applicable to conditions of both plane stress and plane strain.

First, through an example, the principal stresses of numerical specimen with ψ–β = 45°–45° at the crack-initiation stress (corresponding to the point *a* in Figure 12e) were obtained and compared with those based on the Hondros' solution (2α = 12°) as shown in Figure 15. Along the loaded diameter, the tangential and radial stresses ($\sigma_{\theta\theta}$ and σ_{rr}) in the Hondros' solution coincide with the horizontal and vertical stresses (σ_{xx} and σ_{yy}), respectively. It is demonstrated that: (1) the results of numerical modelling follow the overall trend of the theoretical solution that the vertical stresses (σ_{yy}) are compressive and increase with the distance from the centre of the disk; and (2) the horizontal stresses (σ_{xx}) are tensile in the

middle section ($-0.8R < r < 0.8R$) and compressive near the two loading points. However, values of σ_{xx} and σ_{yy} obtained from numerical modelling fluctuate greatly around those predicted by the Hondros' solution due to the inherent heterogeneity of particle size distribution and bond strength and the anisotropy induced by weak planes. For example, the tensile stress or shear stress at the weak plane does not exceed the micro-tensile strength (3.5 MPa) or cohesion (25 MPa) of SJC, respectively, while those at the rock matrix can be far higher owing to the higher strength of FJC.

In addition, tensile principal stresses of slate specimens at ψ–β = 45°–45°, 0°–0° and 0°–90° obtained through the DEM, and those of isotropic rock specimen along the loaded diameter obtained by the continuum method [50] are compared in Figure 16. In general, the tensile stress distributions on end surfaces and the middle plane are different, particularly near two loading points, which is to some extent in agreement with that by the continuum method. As seen in Figure 16d, the tensile stresses on the surface are higher than those on the middle plane. This discrepancy is attributed to the shape effect of the disk specimen [49]. In the isotropic material, the stress distributions on the two end surfaces are symmetrical with respect to the middle plane and taken as identical [49, 50, 52]. However, in this transversely isotropic specimen, there exists a difference in stress distributions on the two end surfaces. This difference is most significant in the specimen at ψ–β = 0°–90°, less at ψ–β = 45°–45° and least at ψ–β = 0°–0°, which is dependent on the degree of influence imposed by the weak planes.

5. Conclusions

2D modelling is incapable of analysing many practical anisotropic problems, such as the borehole instability in oblique wells excavated in anisotropic formations, estimation of elastic properties and reproduction of cross-weak-plane fracture growth in transversely isotropic rocks. Thus, a 3D DEM model for slate, a transversely isotropic rock, was constructed combining FJC and SJC models to investigate the influence of foliation orientation on its tensile behaviour under indirect tensile conditions. A new calibration procedure was proposed for the DEM

modelling of transversely isotropic rock. Based on the numerical analysis in this paper, the following conclusions can be drawn:

(1) At $0° \leq \psi \leq 30°$, the tensile strength of slate sample is independent of ψ and increases with β, but at $45° \leq \psi \leq 90°$, variations in its tensile strength are insensitive to β, with tensile strength increasing with ψ. The coupling effect of β and ψ is illustrated by the anisotropy ratio map of tensile strength, evident at $30° \leq \psi < 45°$.

(2) The fracture pattern of slate sample under indirect tensile conditions is primarily dependent on ψ, while its fracture process primarily depends on β. The cross-weak-plane fracture growth is evident in specimens at $30° \leq \psi \leq 60°$, but it is not evident in other cases. The fracture of specimen at $0° \leq \psi \leq 60°$ and $0° \leq \beta \leq 15°$ initiates at the center of disk and then propagates towards the loading points, whereas the specimen at the other foliation orientations presents an opposite fracture process.

(3) The proportional variations of micro-cracks at failure with ψ and β well account for the effects of foliation orientation on the tensile strength and failure pattern. It is also found that the portion of tensile cracks formed in the rock matrix is responsible for the tensile strength of specimen.

(4) The introduction of weak planes into isotropic rock model increases both heterogeneity and anisotropy of stress distributions. There exists a difference in principal stress distributions on the two end surfaces of the disk-shaped transversely isotropic specimen, which is dependent on the degree of influence imposed by the weak planes. Taking into full account the foliation orientation, a more reliable solution to the indirect tensile strength for transversely isotropic rocks should be derived in future work.

Acknowledgements

This research was financially supported by the National Natural Science Foundation of China (Grant No. 11772358), and a RIF project (Grant No.: R5037-18F) from Research Grants

Council (RGC) of Hong Kong Special Administrative Region Government (HKSARG) of China.

References

[1] Amadei B. Importance of anisotropy when estimating and measuring in situ stresses in rock. International Journal of Rock Mechanics and Mining Sciences & Geomechanics Abstracts. 1996;33(3):293-325.

[2] Pei J. Strength of transversely isotropic rocks: Massachusetts Institute of Technology, 2008.

[3] Wittke W. Rock mechanics based on an anisotropic jointed rock model (AJRM). John Wiley & Sons, 2014.

[4] Chen Z, He C, Wu D, Xu G, Yang W. Fracture evolution and energy mechanism of deep-buried carbonaceous slate. Acta Geotechnica. 2017:1-18.

[5] Meier T, Rybacki E, Backers T, Dresen G. Influence of Bedding Angle on Borehole Stability: A Laboratory Investigation of Transverse Isotropic Oil Shale. Rock Mechanics and Rock Engineering. 2015;48(4):1535-46.

[6] Blümling P, Bernier F, Lebon P, Derek Martin C. The excavation damaged zone in clay formations time-dependent behaviour and influence on performance assessment. Physics and Chemistry of the Earth, Parts A/B/C. 2007;32(8):588-99.

[7] Tsang CF, Barnichon JD, Birkholzer J, Li XL, Liu HH, Sillen X. Coupled thermo-hydro-mechanical processes in the near field of a high-level radioactive waste repository in clay formations. International Journal of Rock Mechanics and Mining Sciences. 2012;49(31-44.

[8] Ma T, Peng N, Zhu Z, Zhang Q, Yang C, Zhao J. Brazilian Tensile Strength of Anisotropic Rocks: Review and New Insights. Energies. 2018;11(2):304.

[9] Zheng Y, Chen C, Liu T, Song D, Meng F. Stability analysis of anti-dip bedding rock slopes locally reinforced by rock bolts. Engineering Geology. 2019;251(228-40.

[10] Hobbs DW. The tensile strength of rocks. International Journal of Rock Mechanics and Mining Sciences & Geomechanics Abstracts. 1964;1(3):385-96.

[11] Celleri HM, Sánchez M, Otegui JL. Fracture behavior of transversely isotropic rocks with

discrete weak interfaces. International Journal for Numerical and Analytical Methods in Geomechanics. 2018;42(18):2161-76.

[12] Xu G, He C, Chen Z, Wu D. Effects of the micro-structure and micro-parameters on the mechanical behaviour of transversely isotropic rock in Brazilian tests. Acta Geotechnica. 2018;13(4):887-910.

[13] Aliabadian Z, Zhao G-F, Russell AR. Crack development in transversely isotropic sandstone discs subjected to Brazilian tests observed using digital image correlation. International Journal of Rock Mechanics and Mining Sciences. 2019;119(211-21.

[14] Barla G, Innaurato N. Indirect tensile testing of anisotropic rocks. Rock mechanics. 1973;5(4):215-30.

[15] Claesson J, Bohloli B. Brazilian test: stress field and tensile strength of anisotropic rocks using an analytical solution. International Journal of Rock Mechanics and Mining Sciences. 2002;39(8):991-1004.

[16] Tavallali A, Vervoort A. Failure of Layered Sandstone under Brazilian Test Conditions: Effect of Micro-Scale Parameters on Macro-Scale Behaviour. Rock Mechanics and Rock Engineering. 2010;43(5):641-53.

[17] Wang Y, Li C, Hu Y, Mao T. Brazilian Test for Tensile Failure of Anisotropic Shale under Different Strain Rates at Quasi-static Loading. Energies. 2017;10(9):1324.

[18] Duan K, Kwok CY. Evolution of stress-induced borehole breakout in inherently anisotropic rock: Insights from discrete element modeling. Journal of Geophysical Research: Solid Earth. 2016;121(4):2361-81.

[19] Shang J, Duan K, Gui Y, Handley K, Zhao Z. Numerical investigation of the direct tensile behaviour of laminated and transversely isotropic rocks containing incipient bedding planes with different strengths. Computers and Geotechnics. 2018;104(373-88.

[20] Yang S-Q, Yin P-F, Huang Y-H. Experiment and Discrete Element Modelling on Strength, Deformation and Failure Behaviour of Shale Under Brazilian Compression. Rock Mechanics and Rock Engineering. 2019;52(11):4339-59.

[21] Han D, Li K, Meng J. Evolution of nonlinear elasticity and crack damage of rock joint under cyclic tension. International Journal of Rock Mechanics and Mining Sciences. 2020;128(104286.

[22] Debecker B, Vervoort A. Experimental observation of fracture patterns in layered slate. International Journal of Fracture. 2009;159(1):51-62.

[23] Dan DQ, Konietzky H, Herbst M. Brazilian tensile strength tests on some anisotropic rocks. International Journal of Rock Mechanics and Mining Sciences. 2013;58(1-7.

[24] Dan DQ, Konietzky H. Numerical simulations and interpretations of Brazilian tensile tests on transversely isotropic rocks. International Journal of Rock Mechanics and Mining Sciences. 2014;71(53-63.

[25] Ding C, Hu D, Zhou h, Lu j, Ma D, Zhang Y. Brazilian splitting tests of slate considering three-dimensional foliation effect. Chinese Journal of Rock Mechanics and Engineering. 2019;38(2):301-12.

[26] Duan K, Kwok CY. Discrete element modeling of anisotropic rock under Brazilian test conditions. International Journal of Rock Mechanics and Mining Sciences. 2015;78(Supplement C):46-56.

[27] Park B, Min K-B. Bonded-particle discrete element modeling of mechanical behavior of transversely isotropic rock. International Journal of Rock Mechanics and Mining Sciences. 2015;76(243-55.

[28] Wang P, Yang T, Xu T, Cai M, Li C. Numerical analysis on scale effect of elasticity, strength and failure patterns of jointed rock masses. Geosciences Journal. 2016;20(4):539-49.

[29] Xia L, Zeng Y. Parametric study of smooth joint parameters on the mechanical behavior of transversely isotropic rocks and research on calibration method. Computers and Geotechnics. 2018;98(1-7.

[30] Xu G, He C, Chen Z, Su A. Transverse Isotropy of Phyllite Under Brazilian Tests: Laboratory Testing and Numerical Simulations. Rock Mechanics and Rock Engineering. 2018;51(4):1111-35.

[31] Duan K, Kwok C, Pierce M. Discrete element method modeling of inherently anisotropic rocks under uniaxial compression loading. International Journal for Numerical and Analytical Methods in Geomechanics. 2016;40(8):1150-83.

[32] Duan K, Wu W, Kwok CY. Discrete element modelling of stress-induced instability of directional drilling boreholes in anisotropic rock. Tunnelling and Underground Space Technology. 2018;81(55-67.

[33] Min K-B, Thoraval A. Comparison of two-and three-dimensional approaches for the numerical determination of equivalent mechanical properties of fractured rock masses. Tunnel and Underground Space. 2012;22(2):93-105.

[34] Fan X, Li K, Lai H, Xie Y, Cao R, Zheng J. Internal stress distribution and cracking around flaws and openings of rock block under uniaxial compression: A particle mechanics approach.

Computers and Geotechnics. 2018;102(28-38.

[35] Cao R, Cao P, Lin H, Ma G, Chen Y. Failure characteristics of intermittent fissures under a compressive-shear test: experimental and numerical analyses. Theoretical and Applied Fracture Mechanics. 2018;96(740-57.

[36] Cui Y. Effect of joint type on the shear behavior of synthetic rock. Bulletin of Engineering Geology and the Environment. 2018:1-18.

[37] Zhang C, Lin H, Qiu C, Jiang T, Zhang J. The effect of cross-section shape on deformation, damage and failure of rock-like materials under uniaxial compression from both a macro and micro viewpoint. International Journal of Damage Mechanics. 2020:1056789520904119.

[38] Potyondy DO, Cundall PA. A bonded-particle model for rock. International Journal of Rock Mechanics and Mining Sciences. 2004;41(8):1329-64.

[39] Li K, Cheng Y, Fan X. Roles of model size and particle size distribution on macro-mechanical properties of Lac du Bonnet granite using flat-joint model. Computers and Geotechnics. 2018;103(43-60.

[40] Wu S, Xu X. A study of three intrinsic problems of the classic discrete element method using flat-joint model. Rock Mechanics and Rock Engineering. 2016;49(5):1813-30.

[41] Mas Ivars D, Potyondy D, Pierce M, Cundall P. The smooth-joint contact model. Proceedings of WCCM8-ECCOMAS. 2008;2008(8th.

[42] Scholtès L, Donzé F-V. A DEM model for soft and hard rocks: Role of grain interlocking on strength. Journal of the Mechanics and Physics of Solids. 2013;61(2):352-69.

[43] Ding X, Zhang L, Zhu H, Zhang Q. Effect of Model Scale and Particle Size Distribution on PFC3D Simulation Results. Rock Mechanics and Rock Engineering. 2014;47(6):2139-56.

[44] Schöpfer MP, Abe S, Childs C, Walsh JJ. The impact of porosity and crack density on the elasticity, strength and friction of cohesive granular materials: insights from DEM modelling. International Journal of Rock Mechanics and Mining Sciences. 2009;46(2):250-61.

[45] Li K, Cheng Y, Yin Z-Y, Han D, Meng J. Size effects in a transversely isotropic rock under Brazilian tests: laboratory testing. Rock Mechanics and Rock Engineering. 2020.

[46] Li K, Yin Z, Cheng Y, Cao P, Fan X, Meng J. Size effect and anisotropy in a transversely isotropic rock under compressive conditions. International Journal of Rock Mechanics and Mining Sciences. 2020. (submitted for publication)

[47] Park B, Min K-B, Thompson N, Horsrud P. Three-dimensional bonded-particle discrete

element modeling of mechanical behavior of transversely isotropic rock. International Journal of Rock Mechanics and Mining Sciences. 2018;110(120-32.

[48] Fan X, Li K, Lai H, Zhao Q, Sun Z. Experimental and Numerical Study of the Failure Behavior of Intermittent Rock Joints Subjected to Direct Shear Load. Advances in Civil Engineering. 2018:1-19.

[49] Yu Y, Yin J, Zhong Z. Shape effects in the Brazilian tensile strength test and a 3D FEM correction. International Journal of Rock Mechanics and Mining Sciences. 2006;43(4):623-7.

[50] Li D, Wong LNY. The Brazilian Disc Test for Rock Mechanics Applications: Review and New Insights. Rock Mechanics and Rock Engineering. 2013;46(2):269-87.

[51] Hondros G. The evaluation of Poisson's ratio and the modulus of materials of low tensile resistance by the Brazilian (indirect tensile) test with particular reference to concrete. Australian J Appl Sci. 1959;10(3):243-68.

[52] Liao ZY, Zhu JB, Tang CA. Numerical investigation of rock tensile strength determined by direct tension, Brazilian and three-point bending tests. International Journal of Rock Mechanics and Mining Sciences. 2019;115(21-32.

Tables

Table 1 Calibrated micro-parameters of the FJC for simulating the rock matrix of slate.

Micro-parameter	Definition	Value
ρ_v	Bulk density (kg/m^3)	2760
$R_{\min}$	Minimum particle radius (mm)	0.5
$R_{\max} / R_{\min}$	Ratio of maximum to minimum particle radius	1.5
g_{ratio}	Installation gap ratio	0.3
N_r	Number of elements in radial direction	1
N_α	Number of elements in circumferential direction	4
φ_B	Bonded element fraction	0.9
φ_G	Gapped element fraction	0
$\bar{E}_c$	Effective modulus of bond (GPa)	97
$\bar{k}^n / \bar{k}^s$	Ratio of bond normal to shear stiffness	3.0
$\bar{\sigma}_b$	Mean bond tensile-strength $\pm$ SD (MPa)	60 ± 12
$\bar{c}_b$	Mean bond cohesion strength $\pm$ SD (MPa)	180 ± 36
$\bar{\phi}_b$	Friction angle of bond (degrees)	0
μ	Friction coefficient of bond	0.1
E_c	Effective modulus of particle contact (GPa)	97
k^n / k^s	Ratio of particle normal to shear stiffness	3.0
μ_p	Friction coefficient of particle	0.1

Table 2 Calibrated micro-parameters of the SJC for simulating the foliation plane of slate.

Micro-parameter	Definition	Value
$\bar{k}_n$	Normal stiffness (GPa/m)	5800
$\bar{k}_s$	Shear stiffness (GPa/m)	5800
σ_c	Tensile strength (MPa)	3.5
c_b	Cohesion (MPa)	25
μ_c	Friction coefficient	0.7

Figure captions

Figure 1 Fracture patterns after Brazilian testing: front surface (left), rear surface (middle) and fracture section (right) of slate samples at different β: (a) 60°; (b) 75° and (c) 90°.

Figure 2 Construction of transversely isotropic rock model (ψ represents the angle between sample axis and weak plane, and β represents the angle between loading direction and weak plane).

Figure 3 Smooth-joint contact and element of flat-joint contact with: (a) strength envelope and (b) force-displacement relationship.

Figure 4 Structure of foliation planes embedded in slate [45]: (a) the appearance and (b) a thin section image.

Figure 5 Fracture pattern of slate sample at ψ = 90° after Brazilian testing.

Figure 6 Flowchart of calibration process for the three-dimensional FJC-SJC model.

Figure 7 Comparisons between experimental and numerical results of specimens 50 mm in diameter: (a) UCS and (b) apparent Young's modulus at $\beta = \psi$ under uniaxial compression tests (c) BFS at $\psi = 0°$ under Brazilian tests; and (d) the influence of specimen thickness on BFS at $\psi = 0°$ under Brazilian tests.

Figure 8 Arrangement of measurement spheres along the loading plane in the disk-shaped specimen under the Brazilian test. Diameter of measurement spheres l = 2.5 mm.

Figure 9 Comparison among the distribution of experimental tensile strength, numerical BFS and σ_{xx} at the centre of disk.

Figure 10 Influences of (a) β and (b) ψ on BFS of slate samples.

Figure 11 Normalized BFS of slate samples at different β and ψ obtained: (a) in this study; (b) by Ding et al. [25] and (c) by Dan et al. [23].

Figure 12 Stress and micro-crack evolution of slate samples at ψ–β: (a) 0°—0°; (b) 0°—45°; (c) 0°—90°; (d) 45°—0°; (e) 45°—45°; (f) 45°—90° and (g) 90°-X (X can be any value in the range of 0°—90°)

Figure 13 Stress-strain curves and failure patterns of slate specimens at ψ–β: (a) 0°—0°; (b) 0°—45° and (c) 0°—90° observed in laboratory. The No. 4 to 8 transverse strains were measured with a series of horizontal strain gages glued along the loaded diameter of specimen in one of its faces.

Figure 14 Variations of percentage of micro-cracks developed in slate samples with β at ψ: (a) 0°; (b) 15°; (c) 30°; (d) 45°; (e) 60°; (f) 75° and (g) 90°.

Figure 15 Principal stresses of slate specimen at ψ–β = 45°–45° along the loaded diameter obtained by the DEM and the Hondros' solution at the crack-initiation stress (The green dashed circle denotes the disk-shaped specimen)

Figure 16 Tensile principal stresses of slate specimens at ψ–β: (a) 45°–45°, (b) 0°–0° and (c) 0°–90° along the loaded diameter; and (d) tensile principal stresses of isotropic rock specimen along the loaded diameter obtained by the continuum method [50] (The green dashed circle denotes the disk-shaped specimen)

Figure 1

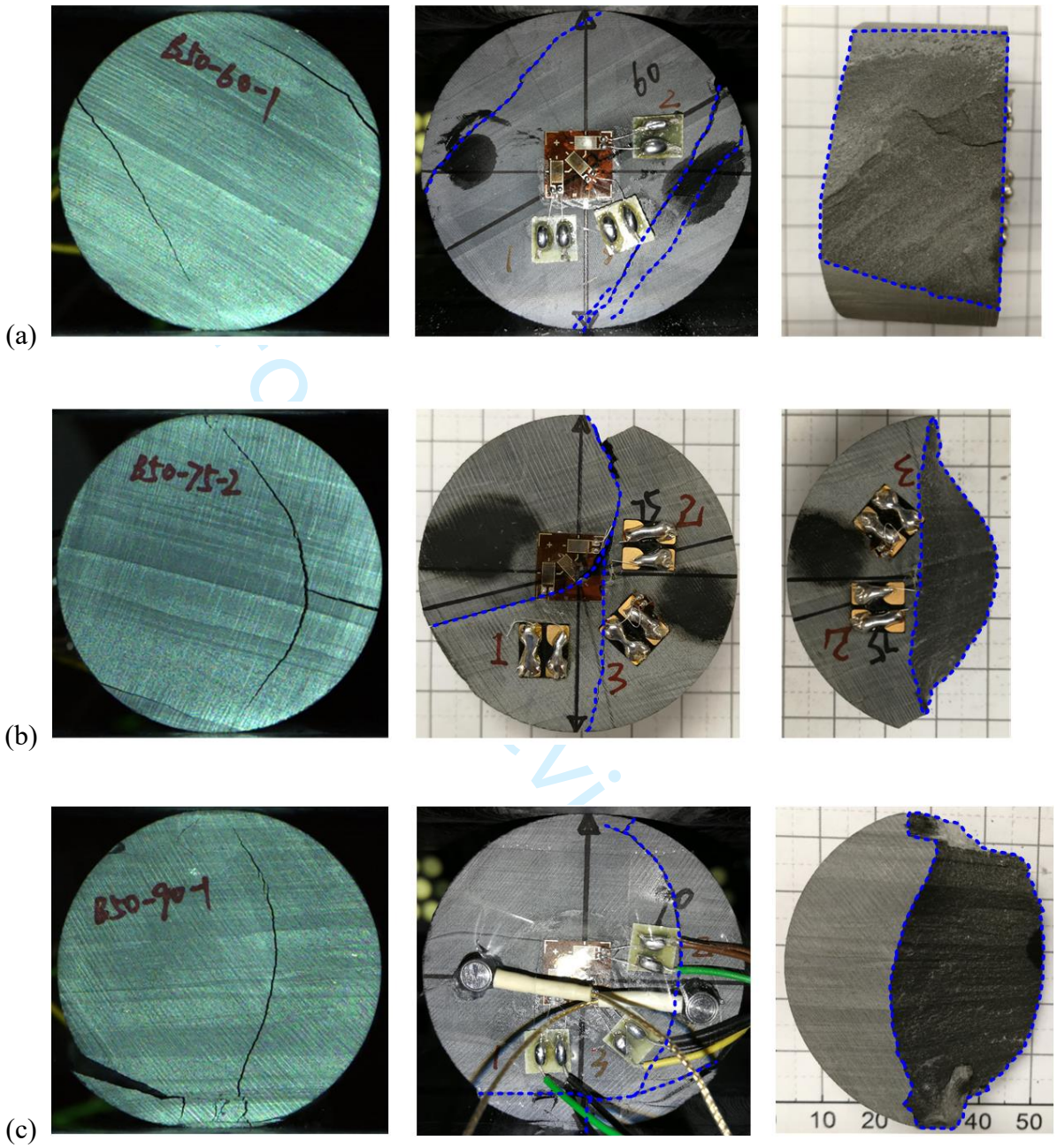

(a)

(b)

(c)

Figure 2

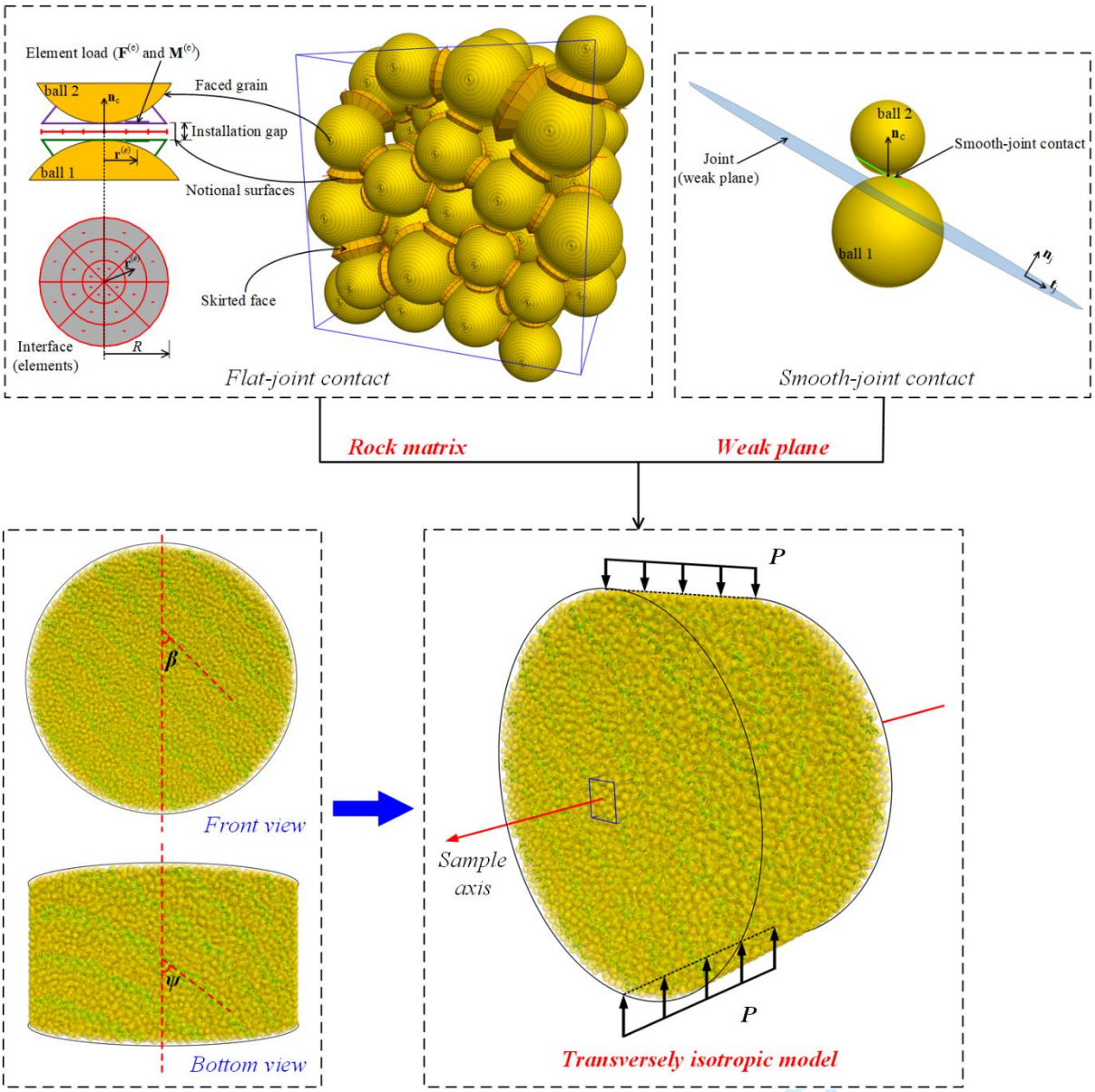
Element load ($\mathbf{F}^{(e)}$ and $\mathbf{M}^{(e)}$)
ball 2
ball 1
Faced grain
Installation gap
Notional surfaces
Skirted face
Interface (elements)
R
Flat-joint contact
Joint (weak plane)
Smooth-joint contact
Rock matrix
Weak plane
β
Front view
ψ
Bottom view
P
Sample axis
Transversely isotropic model

Figure 3

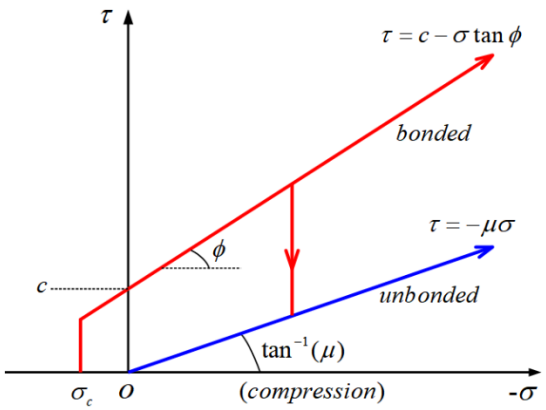

(a)

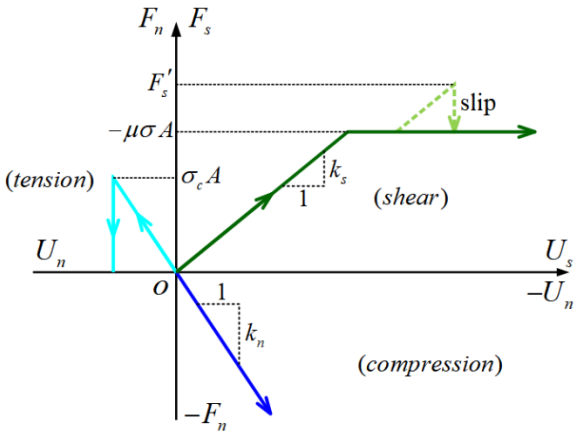

(b)

Figure 4

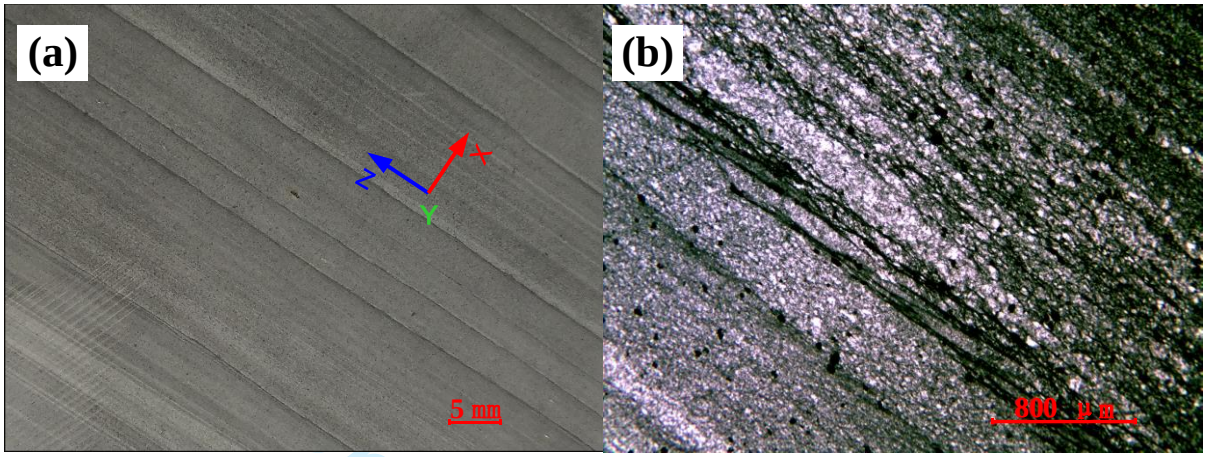

Figure 5

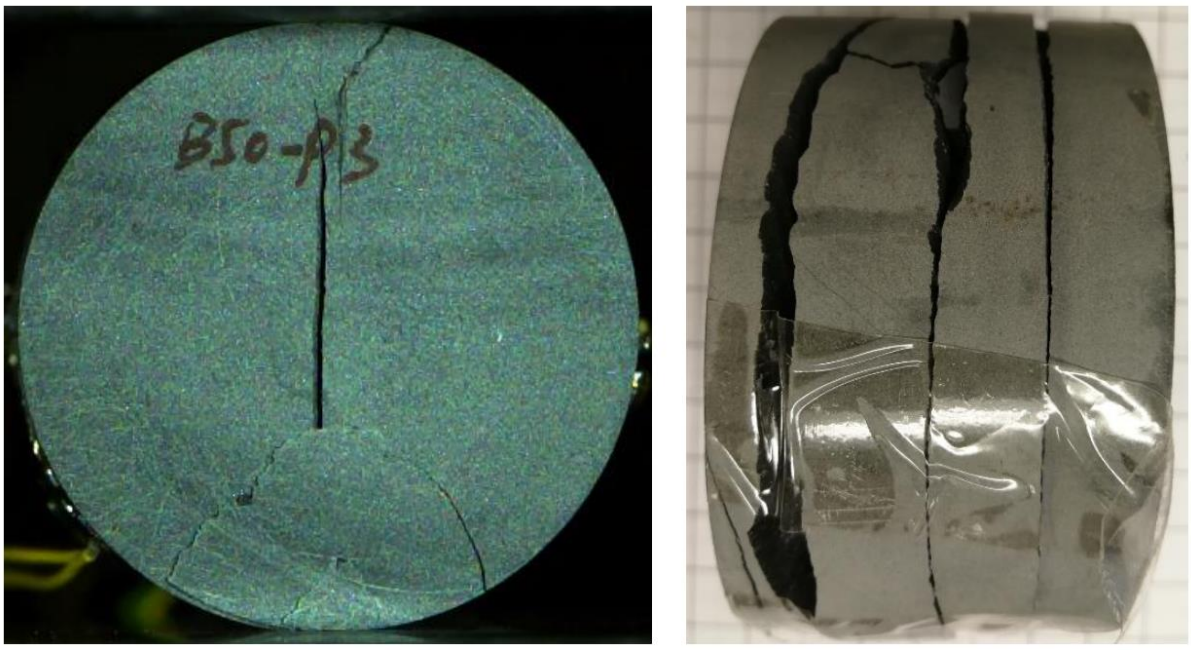

Figure 6

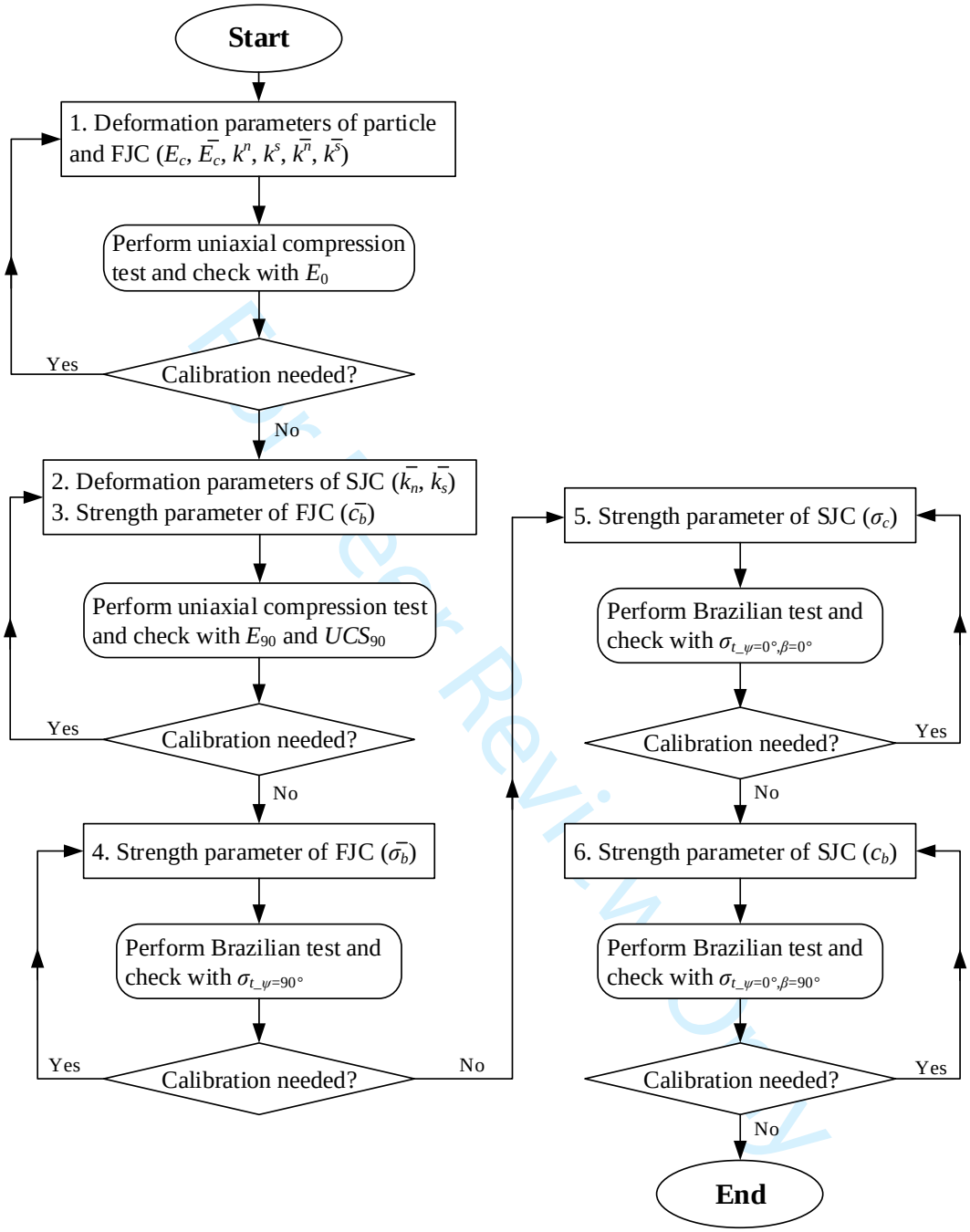

Figure 7

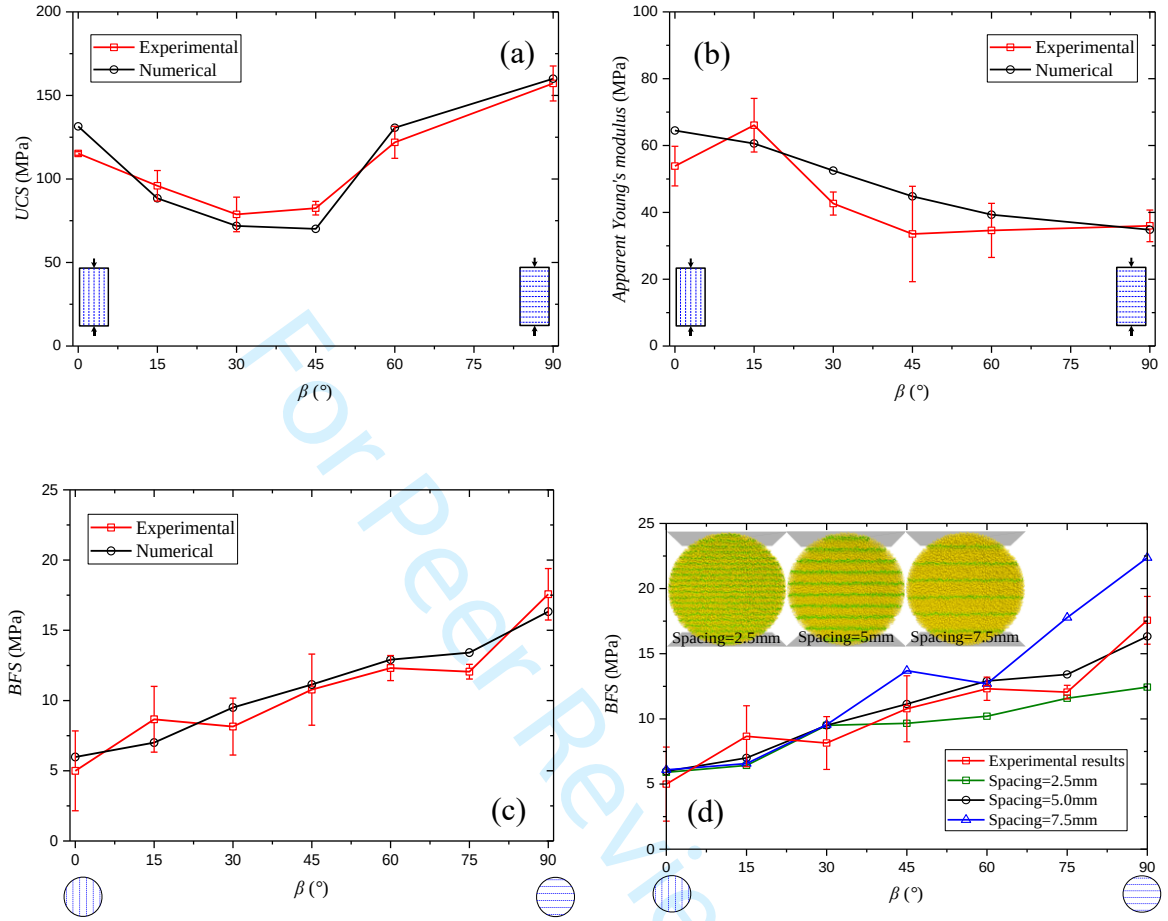

Figure 8

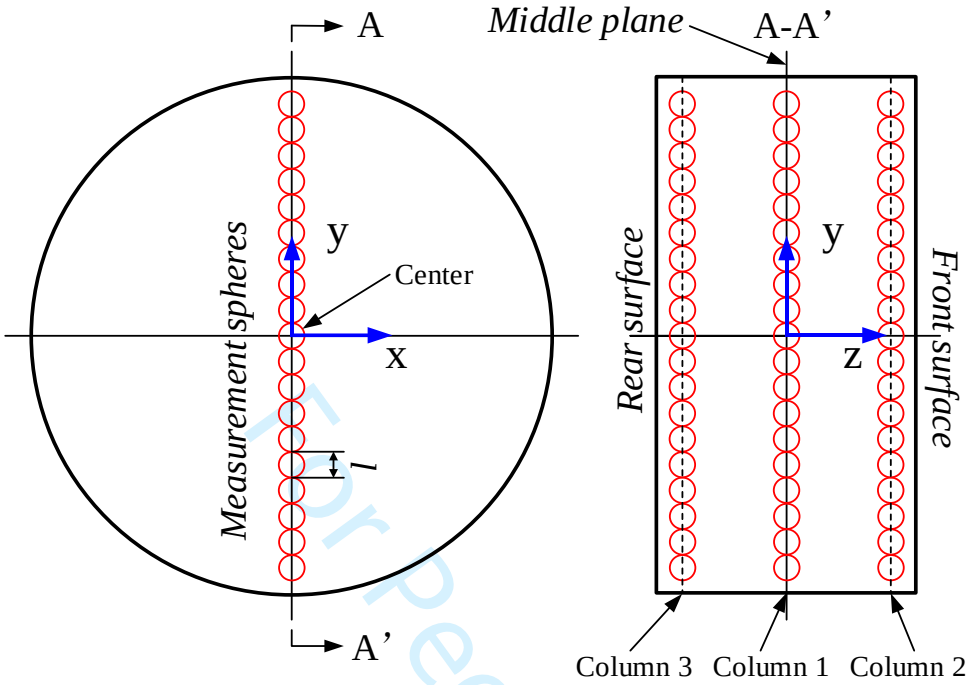

Figure 9

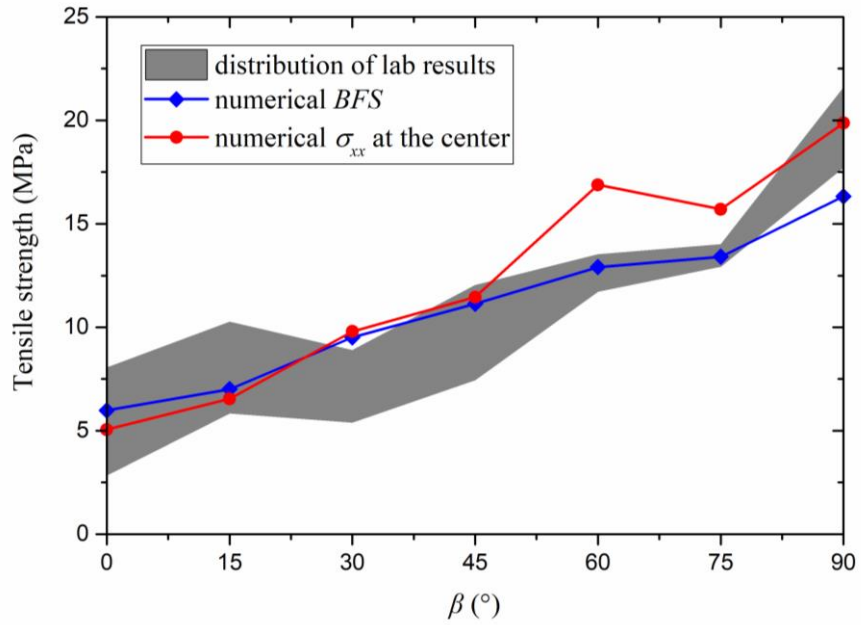

Figure 10

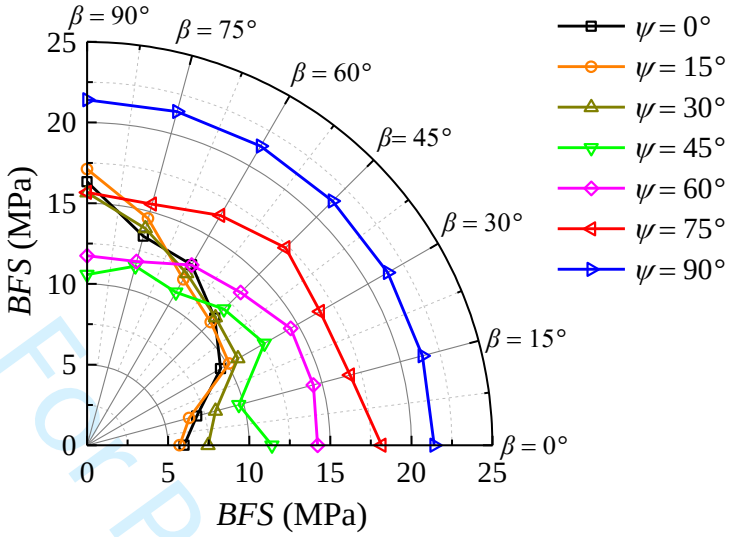

(a)

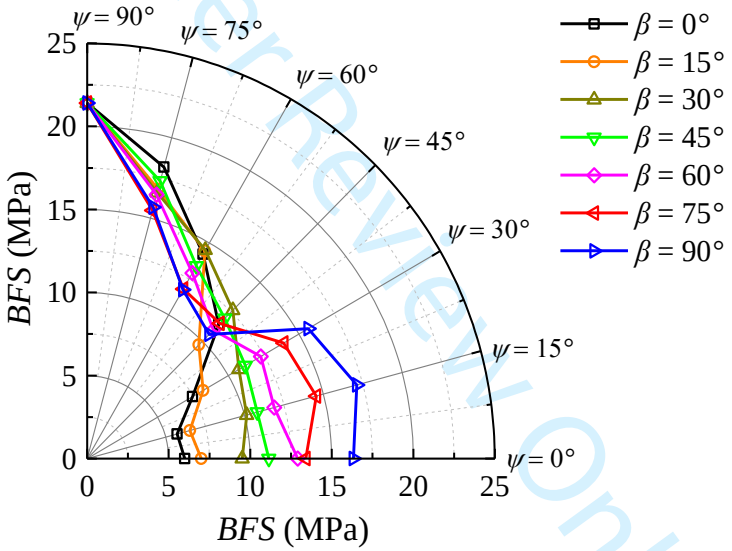

(b)

Figure 11

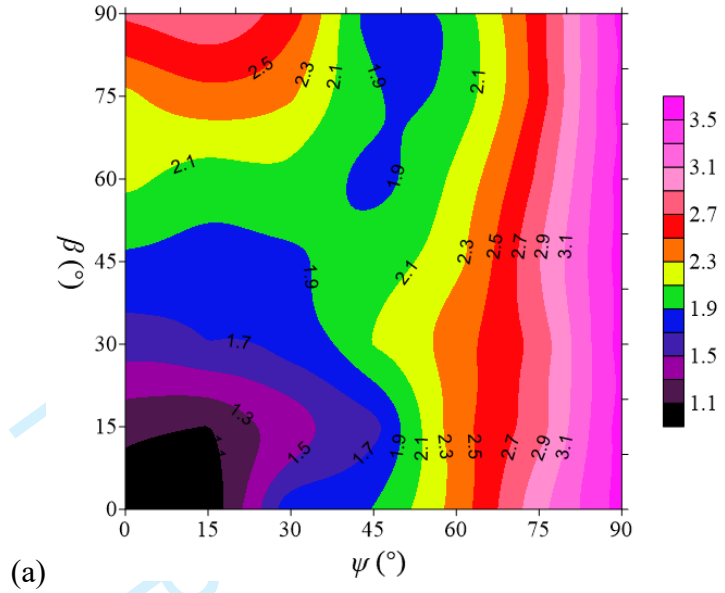

(a)

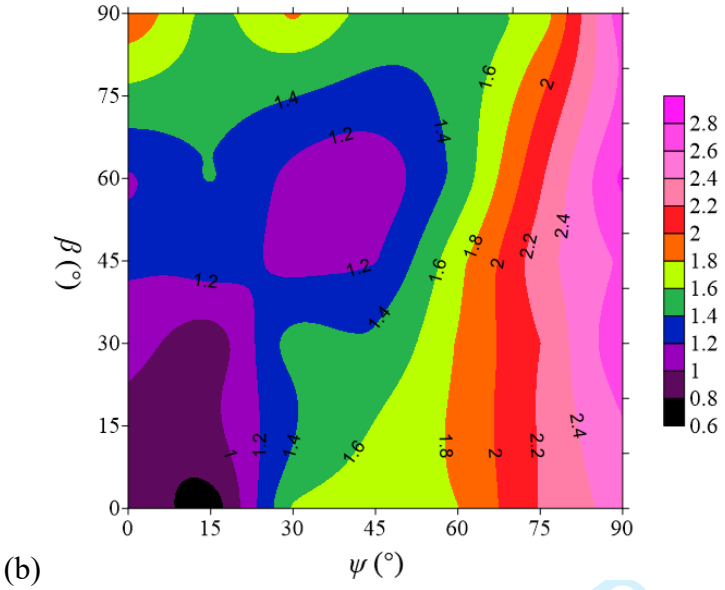

(b)

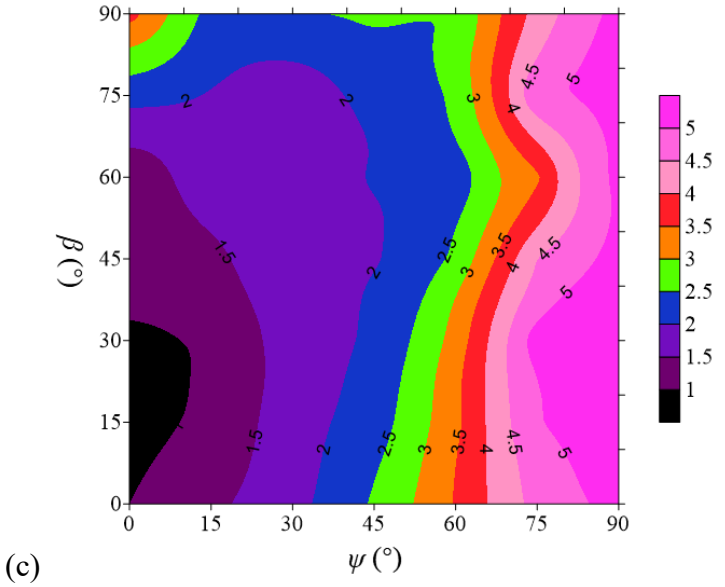

(c)

Figure 12

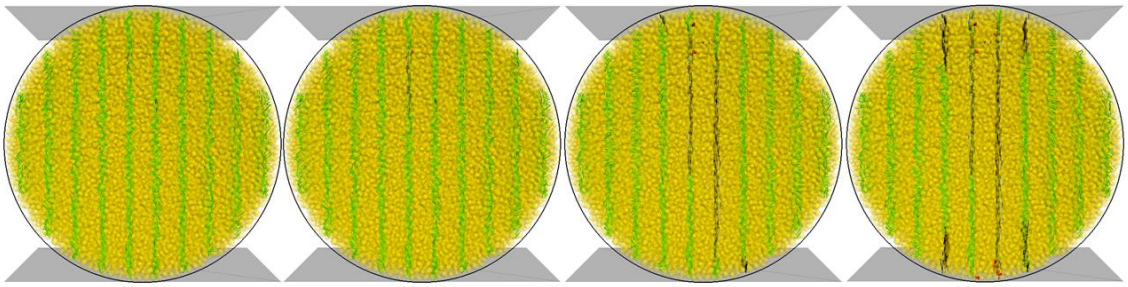

a: 0.55×10^{-3} b: 0.58×10^{-3} c: 0.6×10^{-3} d: 0.63×10^{-3}

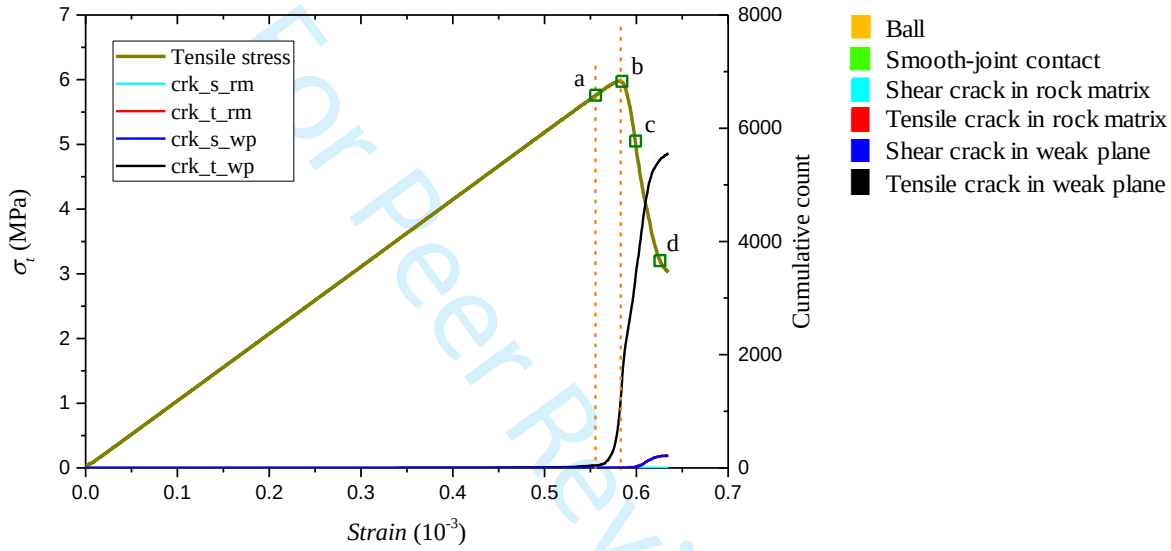

(a)

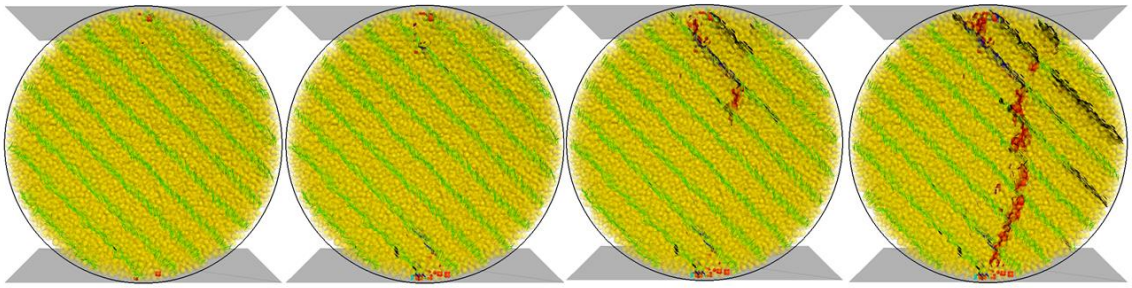

a: 1.0×10^{-3} b: 1.37×10^{-3} c: 1.45×10^{-3} d: 1.55×10^{-3}

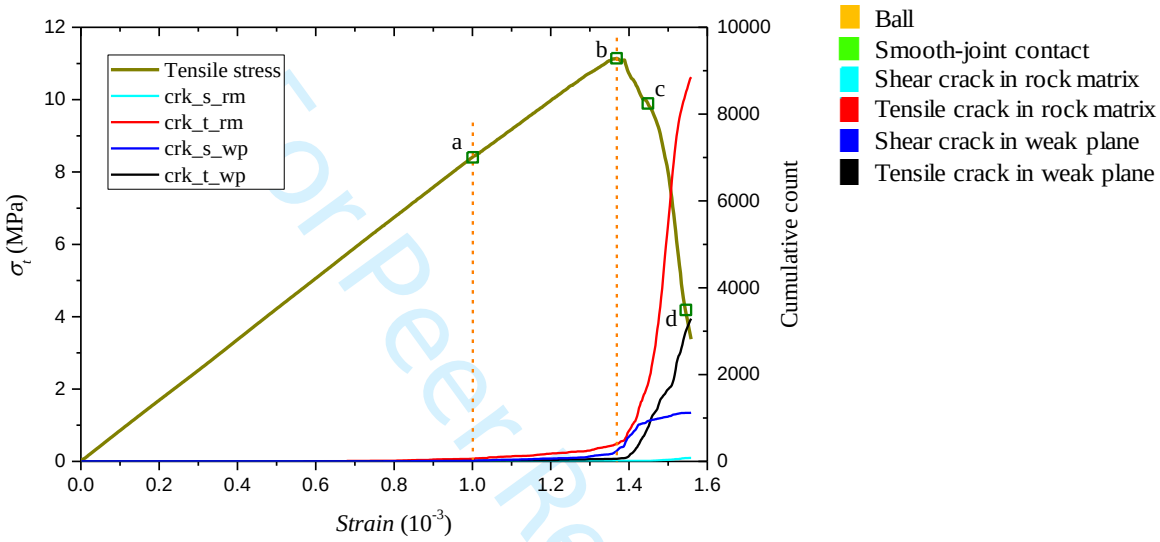

(b)

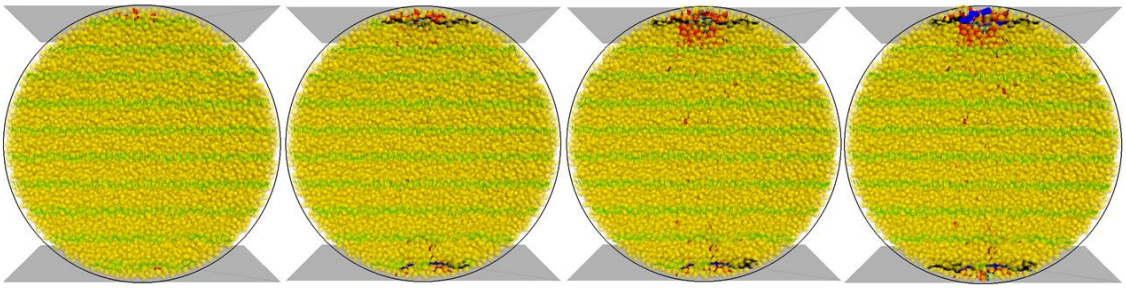

a: 1.4×10^{-3} b: 2.48×10^{-3} c: 3.53×10^{-3} d: 4.86×10^{-3}

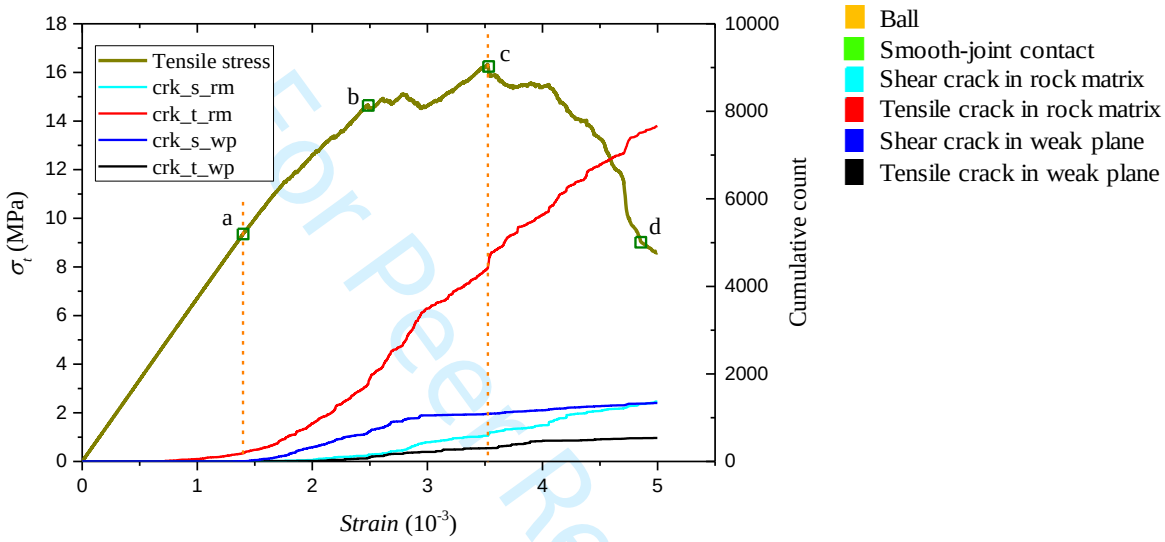

(c)

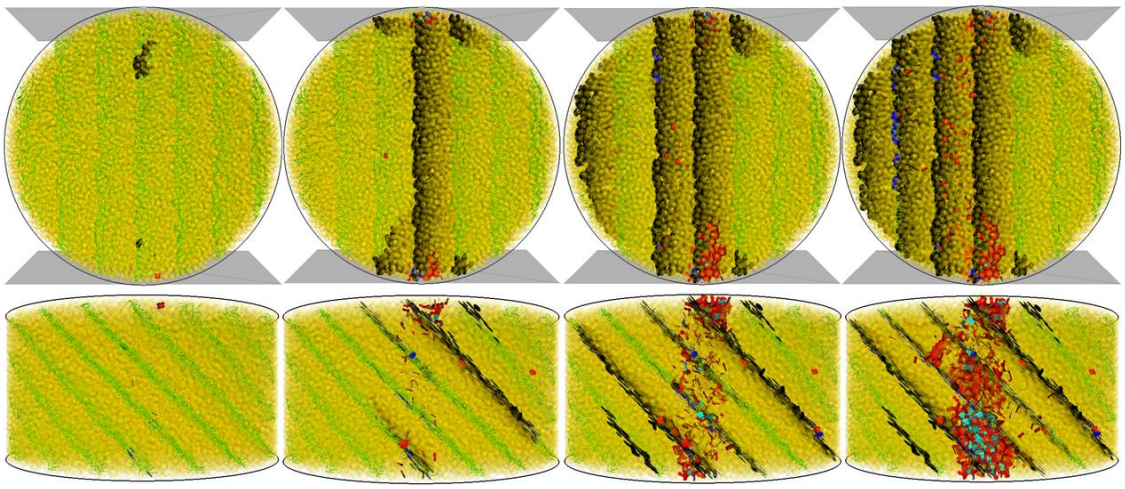

a: 0.75×10^{-3} b: 1.03×10^{-3} c: 1.52×10^{-3} d: 1.98×10^{-3}

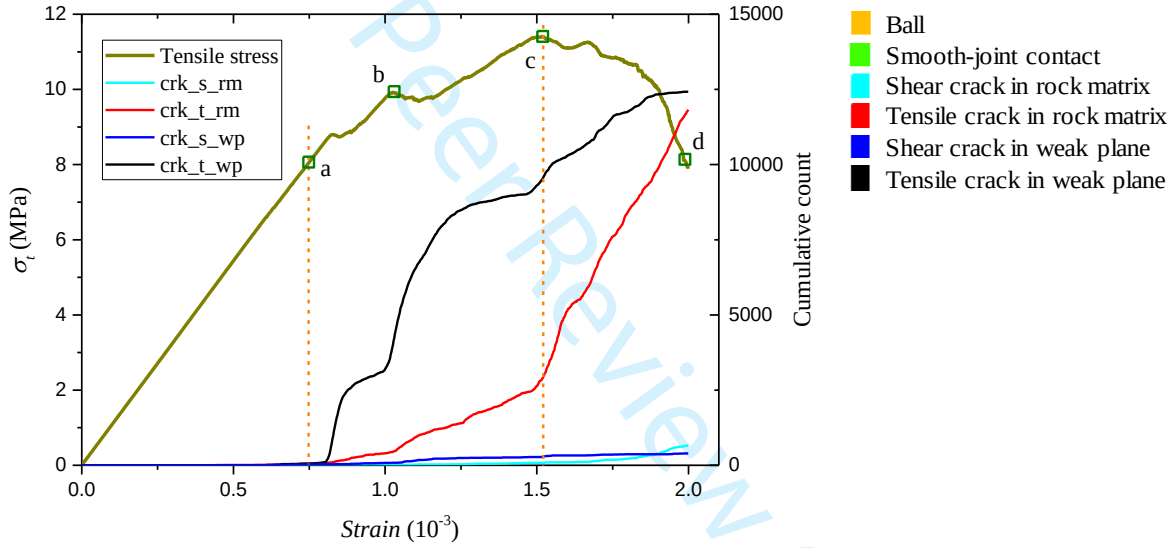

(d)

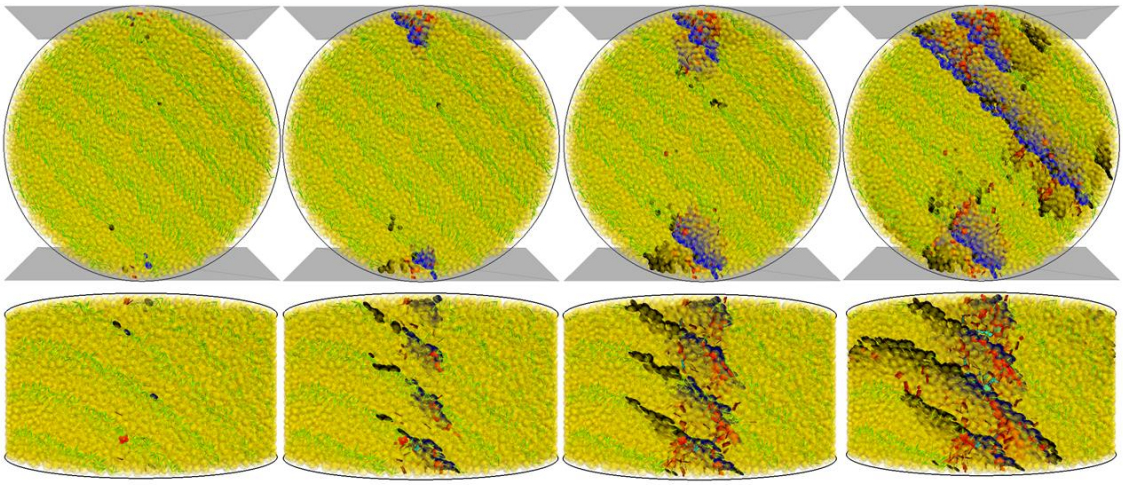

a: 0.86 × 10^{-3} b: 1.19 × 10^{-3} c: 1.57 × 10^{-3} d: 1.85 × 10^{-3}

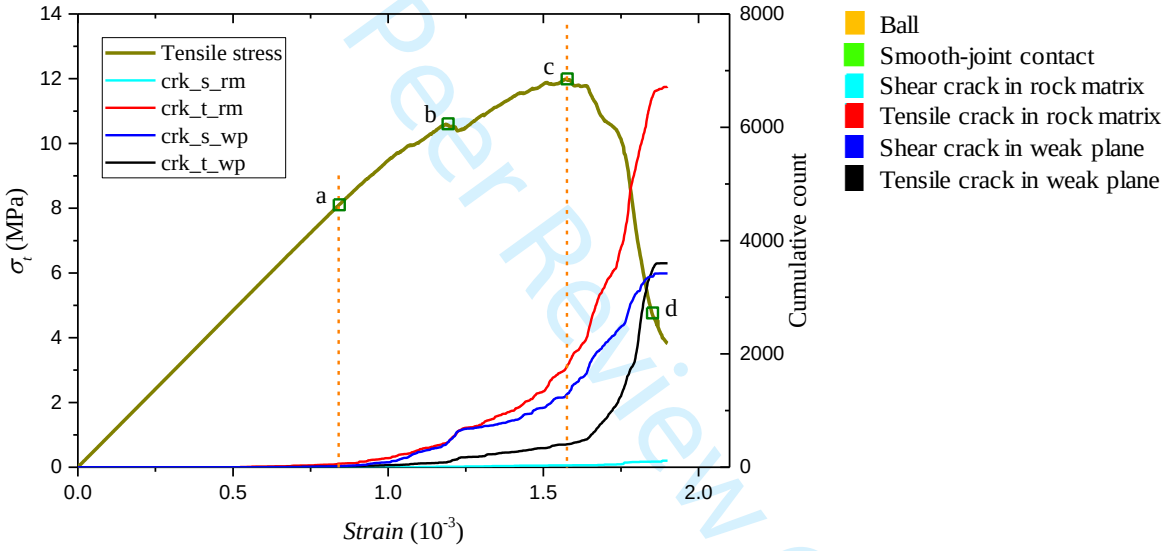

(e)

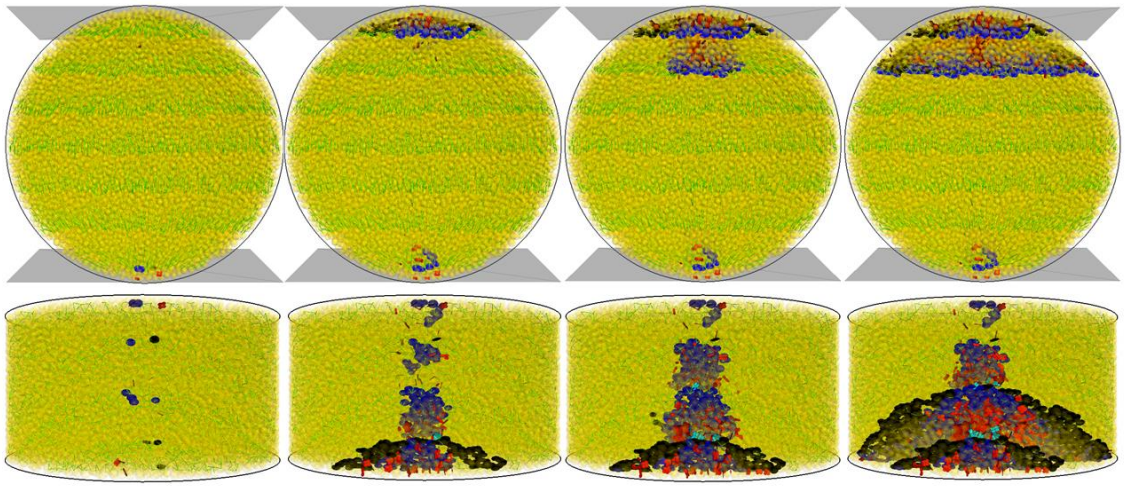

a: 0.87×10^{-3} b: 1.22×10^{-3} c: 1.6×10^{-3} d: 1.8×10^{-3}

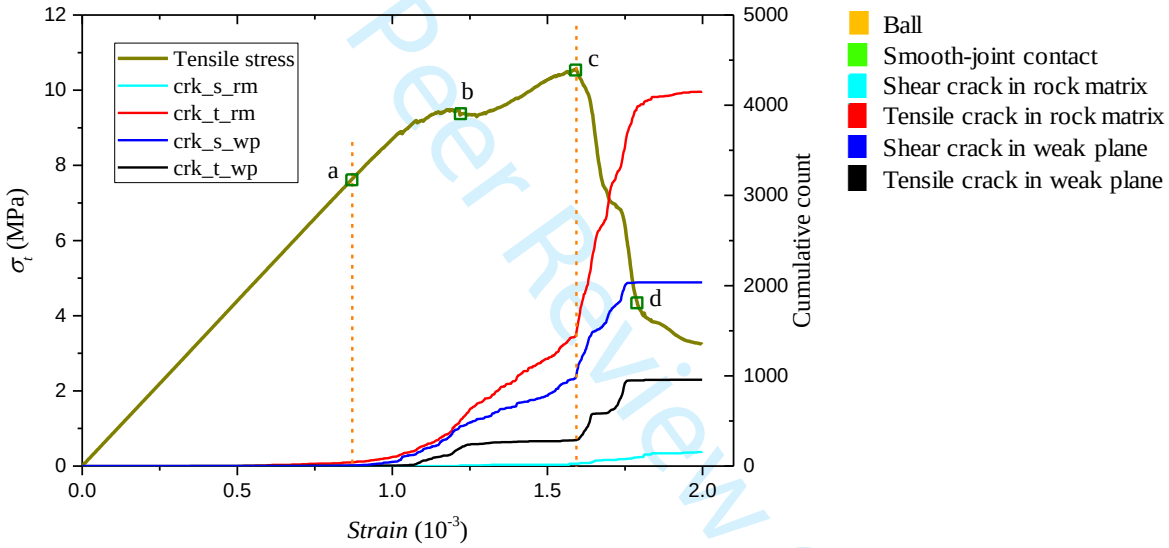

(f)

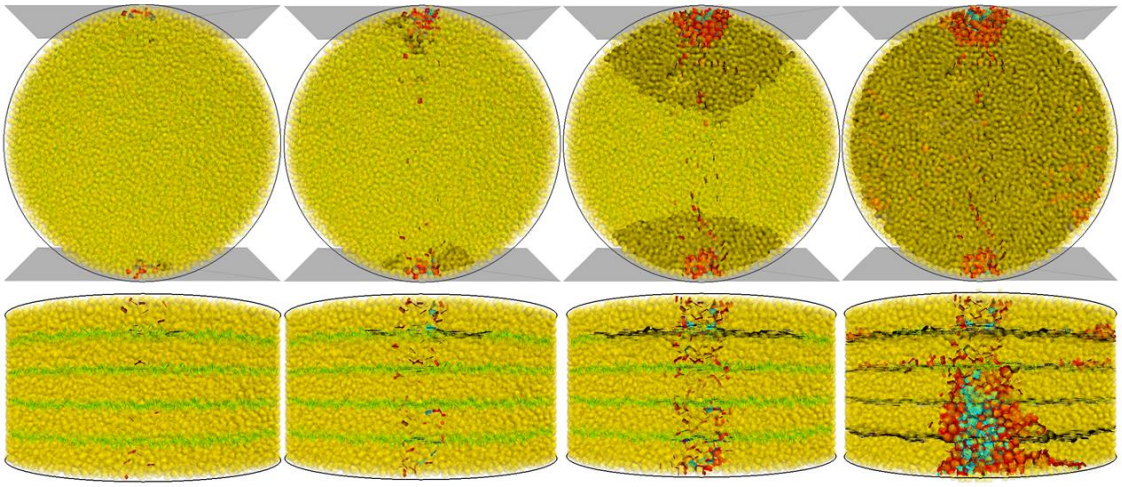

a: 1.0×10^{-3} b: 1.4×10^{-3} c: 1.93×10^{-3} d: 2.44×10^{-3}

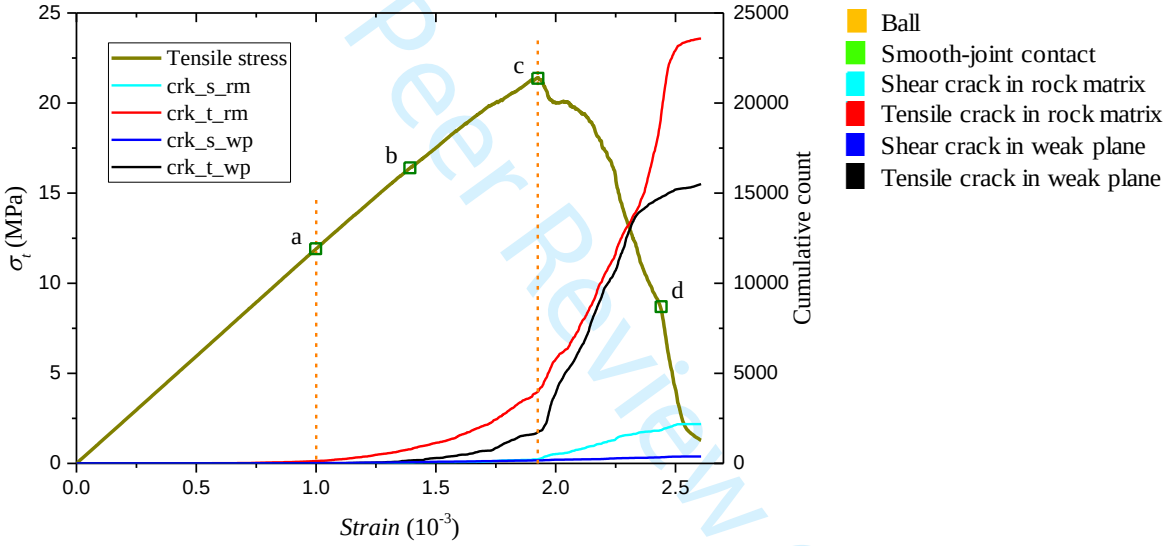

(g)

Figure 13

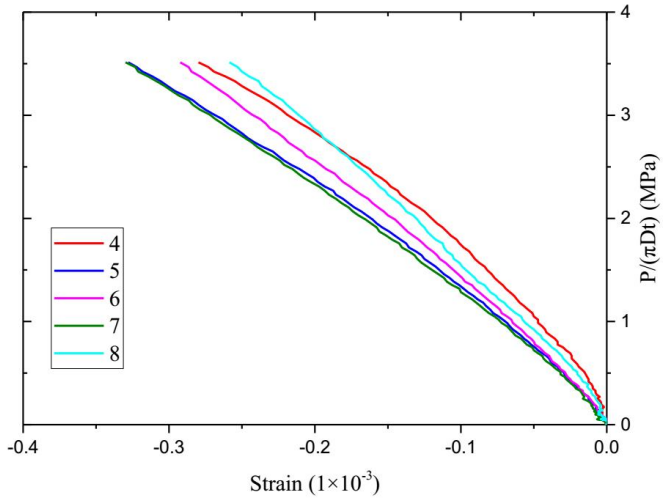

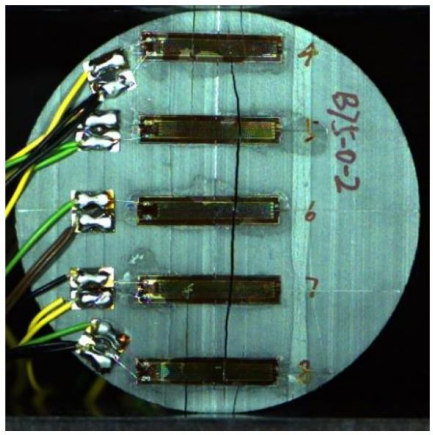

(a)

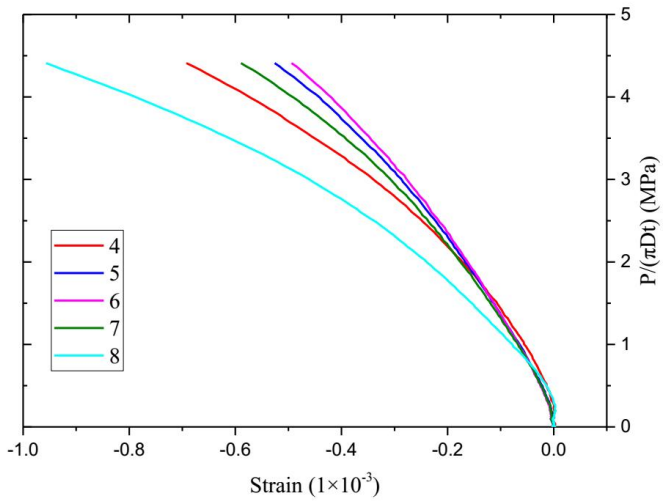

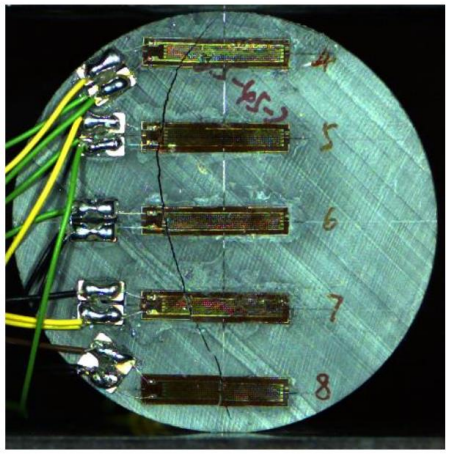

(b)

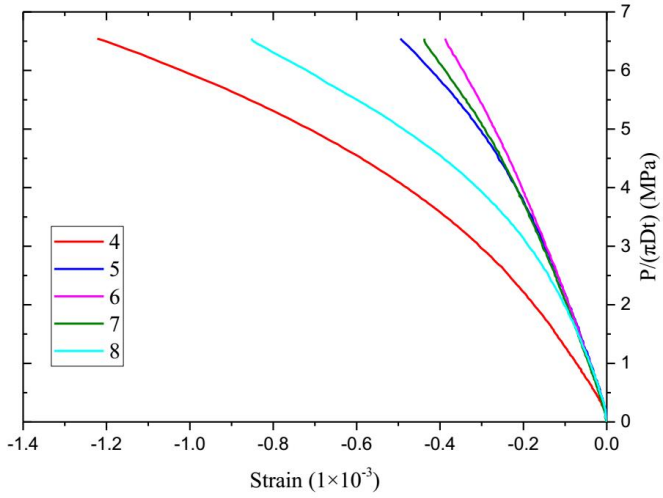

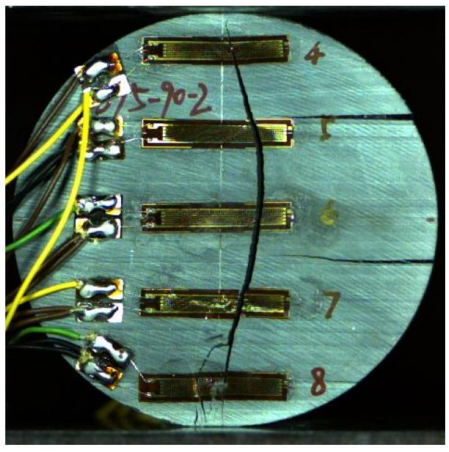

(c)

Figure 14

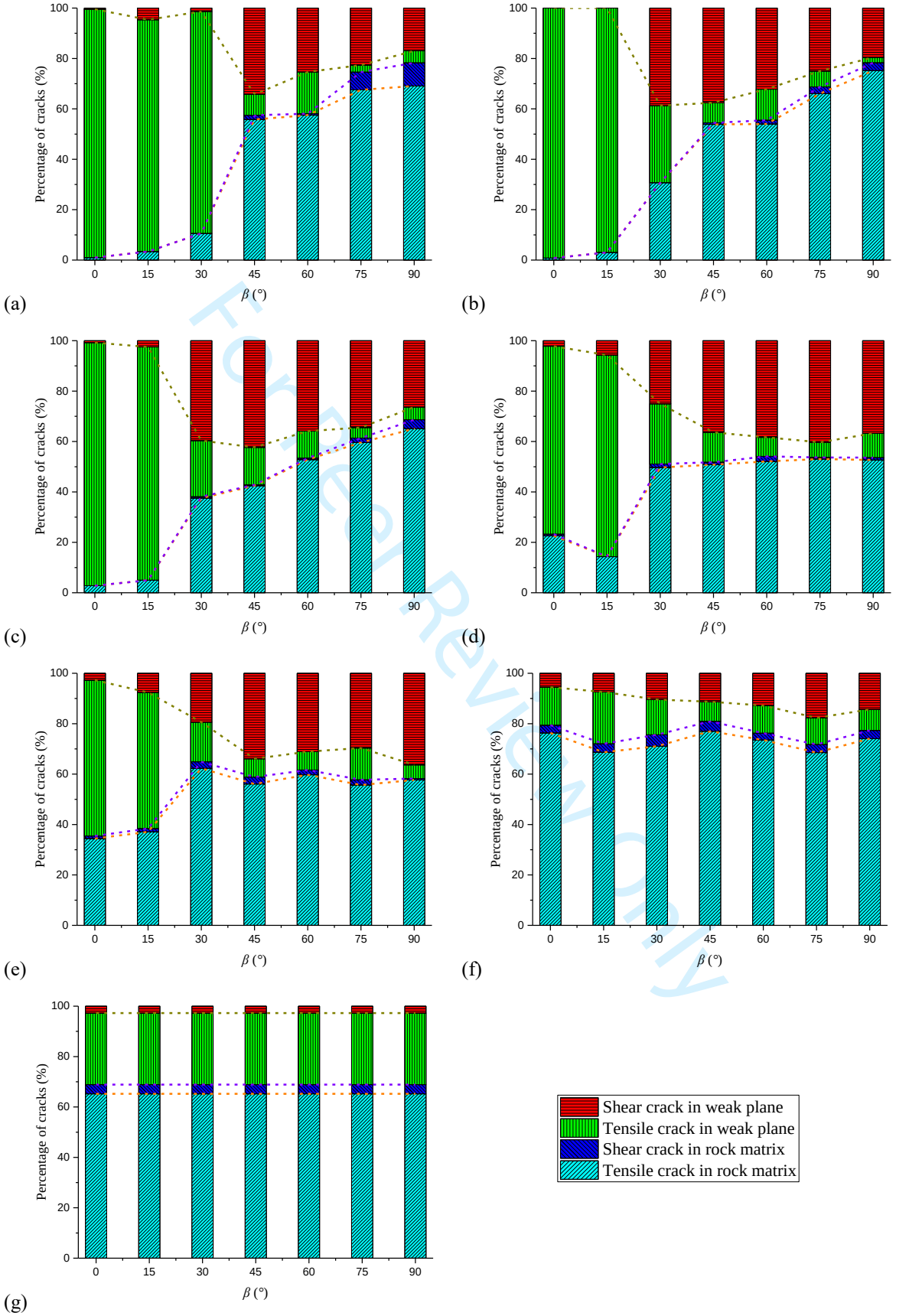

Figure 15

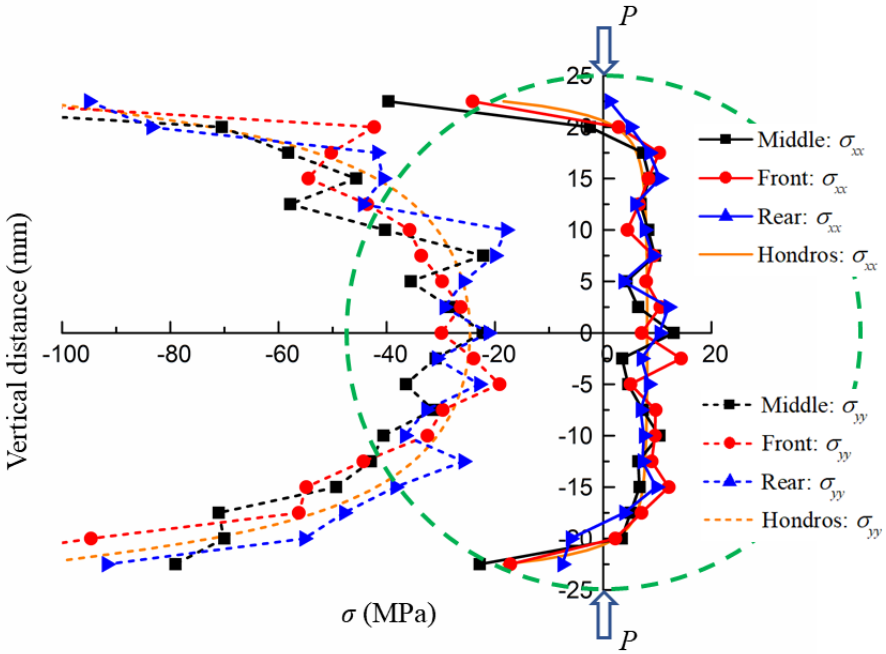

Figure 16